RESEARCH ARTICLE

Key Points:
- Local peaks are quantified and related to Fickian regime proximity
- Local peak frequency is shown to be a function of hydrogeologic parameters
- Average BTC and local slopes differ, sometimes by several orders of magnitude

Correspondence to:
E. R. Siirila-Woodburn,
erwoodburn@lbl.gov

On the formation of multiple local peaks in breakthrough curves

Erica R. Siirila-Woodburn[1,2], Xavier Sanchez-Vila[1], and Daniel Fernàndez-Garcia[1]

[1]GHS, Department of Geotechnical Engineering and Geosciences, Universitat Politècnica de Catalunya, Barcelona, Spain, [2]Now at Earth Sciences Division, Lawrence Berkeley National Laboratory, Berkeley, California, USA

Abstract The analysis of breakthrough curves (BTCs) is of interest in hydrogeology as a way to parameterize and explain processes related to anomalous transport. Classical BTCs assume the presence of a single peak in the curve, where the location and size of the peak and the slope of the receding limb has been of particular interest. As more information is incorporated into BTCs (for example, with high-frequency data collection, supercomputing efforts), it is likely that classical definitions of BTC shapes will no longer be adequate descriptors for contaminant transport problems. We contend that individual BTCs may display multiple local peaks depending on the hydrogeologic conditions and the solute travel distance. In such cases, classical definitions should be reconsidered. In this work, the presence of local peaks in BTCs is quantified from high-resolution numerical simulations in synthetic fields with a particle tracking technique and a kernel density estimator to avoid either overly jagged or smoothed curves that could mask the results. Individual BTCs from three-dimensional heterogeneous hydraulic conductivity fields with varying combinations of statistical anisotropy, heterogeneity models, and local dispersivity are assessed as a function of travel distance. The number of local peaks, their corresponding slopes, and a transport connectivity index are shown to strongly depend on statistical anisotropy and travel distance. Results show that the choice of heterogeneity model also affects the frequency of local peaks, but the slope is less sensitive to model selection. We also discuss how solute shearing and rerouting can be determined from local peak quantification.

1. Introduction

While breakthrough curve (BTC) analysis is a traditional tool in hydrogeology to obtain hydraulic parameters, in recent years, emphasis has been placed on analyzing the shape of the receding portion of the curve [*Haggerty et al.*, 2000; *Dentz and Berkowitz*, 2003; *Zhang et al.*, 2007; *Willmann et al.*, 2008; *Fernàndez-Garcia et al.*, 2009; *Becker and Shapiro*, 2000; *Pedretti et al.*, 2013]. Ongoing questions are: what is the most characteristic shape of the receding portion of the BTC, can we define it mathematically, and what is the relationship between the receding portion of the BTC and physical aquifer parameters and/or processes [e.g., *Bijeljic and Blunt*, 2006; *Willmann et al.*, 2008; *Dentz and Bolster*, 2010; *Pedretti et al.*, 2013, 2014; *Zhang et al.*, 2013]. A number of field and laboratory observations have found a late-time behavior of BTCs with a constant slope in log-log space, and thus it has been hypothesized that a power law behavior is representative of curves in real aquifers [*Farrell and Reinhard*, 1994; *Werth et al.*, 1997; *Haggerty et al.*, 2002; *Schumer et al.*, 2003; *Fernàndez-Garcia et al.*, 2004]. In the investigation of these questions and other involving anomalous transport, late-time BTCs are usually assumed to be monotonic. That is, local peaks in the BTC are not considered so that a local increase or decrease (in time) of BTC slope is disregarded.

In fact, a number of studies have shown that multipeak BTCs do exist [e.g., *Mallants et al.*, 1994]. The presence of fractured media in both numerical simulations [e.g., *Moreno and Tsang*, 1991] and field campaigns [*Andersson et al.*, 1993; *Frost and Davison*, 1994; *Thorbjarnarson and Mackay*, 1994; *Rudolph et al.*, 1996; *Day-Lewis et al.*, 2004] have also shown the emergence of multimodal BTCs. Bimodal BTC peaks are common, and have been observed in many previous analyses [e.g., *Coppola et al.*, 2009; *Bellin et al.*, 1991; *Quinodoz and Valocchi*, 1993; *Michalak and Kitanidis*, 2000], where results are attributed to dual-domain permeability fields and kinetic sorption in nonconservative solutes. Bimodal peaks in field campaigns can also result due

to rainfall dilution [e.g., *Göppert and Goldschneider*, 2008]. Although the focus of this paper is at the field scale, double peak BTCs have also been reported at the pore scale [*Bolster et al.*, 2014].

From the growing body of evidence showing local peaks, we contend that local peaks in BTCs exist and should be considered, but are sometimes not reported for a number of reasons. For example, when BTCs are obtained from actual measurements, subsampling may mask nonmonotonicity, or small peaks may be reported as measurement errors and thus smoothed out or removed. When numerical analyses of synthetic aquifers are performed, the simulation methods used may yield artificially monotonous curves. For example, BTCs obtained from Eulerian methods tend to become oversmoothed, suffering from numerical dispersion as a function of the cell size [e.g., *LaBolle et al.*, 1996; *Salamon et al.*, 2006]. Likewise, while Lagrangian methods based on particle tracking are considered favorable in this respect, they can also suffer from artificial oscillations in the BTC stemming from the reconstruction of concentrations from a limited number of particles [e.g., *Kinzelbach*, 1988; *Salamon et al.*, 2006; *Fernàndez-Garcia and Sanchez-Vila*, 2011; *Boso et al.*, 2013; *Pedretti and Fernàndez-Garcia*, 2013]. Moreover, in most cases individual BTCs are reported in terms of ensemble averages, thus practically eliminating the presence of local maxima in either the advancing or receding limbs of the curve. In these cases, effects related to individual plumes have been averaged out. In reality, only a single realization of heterogeneity exists, and typically the plume is unable to sample the flow field at once, resulting in irregular fingering of the plume. Recently, *Le Borgne et al.* [2013] described this phenomenon as the formation of lamella-like topology, where as travel distance increases, mixing results in diffusive coalesce of these localized fingers and transport behavior behaves closer to the ensemble-mean.

Unimodal assessments of BTCs may no longer suffice with two major advancements in the field of hydrogeology: (1) the increase of high-frequency data and the progression of data collection techniques that diminish the problems of under-sampled BTCs [e.g., *Berman et al.*, 2009; *Tyler et al.*, 2009]; and (2) advancements in supercomputing and numerical simulation allowing for higher resolution of flow and transport problems [e.g., *Kollet et al.*, 2010; *Hammond et al.*, 2014]. As more information is incorporated into BTCs and/or they are obtained in more spatial locations, it is likely that classical definitions of BTC shapes will no longer be adequate descriptors for future treatment of contaminant transport problems. The need for alternative BTC descriptors is partially motivated by the need for integration of hydrogeologic advancements in environmental management decisions. Recent work has shown that time dependence in environmental concentrations is imperative in accurately assessing environmental and human health risk [*Siirila and Maxwell*, 2012a, 2012b; *Kumar et al.*, 2013; *Rodak et al.*, 2013]. Thus, while traditionally the peak environmental concentration is only considered, these recent works suggest the entire BTC should be considered in risk analysis. Depending on the length of the exposure duration and when considering the entire BTC, discrepancies in the environmental concentration at a given time could differ if local peaks were considered.

In this work, the presence of multiple peaks in BTCs is assessed from high-resolution numerical simulations with particle tracking techniques, introducing a kernel density estimator to avoid the impact of using a finite number of particles. Individual realizations of three-dimensional heterogeneous hydraulic conductivity fields with varying combinations of statistical anisotropy, heterogeneity models, and local dispersivity are utilized to test for mechanisms of physical mass transfer. BTCs of nonreactive solutes are analyzed for the presence of local maxima/minima, a question which has received little to no attention in the literature BTCs are also analyzed for the corresponding slope of the receding limb of the curve as a function of travel distance and number of integral scales traveled. The design of this numerical experiment allows for the discussion of BTC evolution in terms of not only the quantity of local peaks, but also how knowledge of local peak quantity and slope relates to pre-Fickian transport.

2. Methodology

Large-extent (10 km), finely discretized (cm scale vertical, m scale horizontal) aquifers are simulated to ensure an accurate representation of different scales of heterogeneity (see Table 1). Saturated aquifer flow is simulated using the parallel, three-dimensional groundwater model ParFlow [*Ashby and Falgout*, 1996; *Jones and Woodward*, 2001; *Kollet and Maxwell*, 2006]. Nonreactive solute transport is simulated with the Lagrangian particle tracking model SLIM-FAST [*Maxwell*, 2010] and a bilinear velocity interpolation [*LaBolle et al.*, 1996]. Each flow field is composed of approximately 184 million cells, necessitating the use of parallel high-performance computing. Two constant head boundaries at $x = 0.0$ (m) and $x = 10,002$ (m) drive a

Table 1. Flow and Transport Parameters

Parameter	Value	Units
Domain size (x, y, z)	$(10{,}002 \times 501 \times 99)$	(m)
Cell discretization (Δx, Δy, Δz)	$(3.0 \times 3.0 \times 0.3)$	(m)
Number of cells (nx, ny, nz)	$(3334 \times 167 \times 330)$	(-)
Centered location of source (x, y, z)	$(250.0, 250.0, 50.0)$	(m)
Number of particles	400,000	(-)
Porosity	$\theta = 0.3$	(-)
x distance between planes	$P_{\Delta x} = 316.66$	(m)
x plane locations (x_1, x_2, . . ., x_{25})	$(566.6, 883.3, . . ., 8166.6)$	(m)
y, z plane locations (y, z)	$(0–501, 0–99)$	(m, m)
Change in head and gradient	$\Delta h = 25.0$	(m)
	$J = 0.0025$	(-)
BTC time step (ts)	10	(d)

groundwater gradient, while all other boundaries are no-flow (see Figure 1 for flow domain schematic and Table 1 for parameters). A 10.0 (m) cubic source of 400,000 particles is instantaneously released, then tracked as a function of time at 25 down-gradient planes perpendicular to the mean flow direction (P_1–P_{25}). Each plane is discretely located, spaced evenly in the x direction along the mean flow length, where the distance between each plane is $P_{\Delta x} = 316.66$ (m) (see Figure 1). As described in sections 2.3 and 2.4, these 25 planes are used to quantify aquifer transport connectivity, the number of local peaks in the BTC, and the local peak slope as a function of travel distance.

While a point source and a planar sampling area were adapted in our methodology, a larger source with a point sampling area (and other combinations of planar versus point sources and sampling areas) could easily be implemented in future studies. A larger source zone would likely result in fewer peaks in the BTC as more preferential flow pathways would converge with the bulk of the solute plume. Unlike the use of a point sampling area, a planar sampling area was selected as it allows for tracking of the entire plume. While the disadvantage of a planar sampling area is the lack of distinction between breakthrough locations at a given time, the ability to track not only a subset of the plume's streamlines intersecting the sampling location but rather the entire plume, was the purpose in selecting this numerical setup. An alternative sampling method considering both local and planar techniques was proposed by *Vanderborght and Vereecken* [2001], which involves the upscaling of local, normalized BTCs to a reference plane.

2.1. Generation of Heterogeneous Flow Fields

The use of geostatistically based heterogeneity models to simulate physical heterogeneity is of interest in this analysis, as the shape of the BTC (number of local peaks and slope) will likely differ given different models, even if the global statistics are the same. Two heterogeneity models, a truncated Gaussian, TG, and a facies model, F, are used to simulate three-dimensional, spatially correlated heterogeneous K fields of equivalent global univariate statistics. In this study, truncated Gaussian random fields are generated internally in ParFlow using the turning bands algorithm [*Tompson et al.*, 1989], which enforces a semivariogram function through rotation of 250 one-dimensional lines through space, and where each value in the random field is a weighted average of values contained within each band. An exponential model is used to define spatial correlation of hydraulic conductivity, K (m d^{-1}). The resulting K field is a continuous distribution where high and low values of K are inherently isolated in nature [*Koltermann and Gorelick*, 1996]. In contrast, a facies K field distribution is discrete, and high and low K values are not necessarily isolated. Facies fields are generated using transition probability indicator simulations (T-PROGS) [*Carle and Fogg*, 1996, 1997; *Carle*, 1999] which utilizes a Markov chain model with cokriging and a final quenching step in the interpolation scheme. Three discrete facies are chosen to populate the K field: High, Fill, and Low. The corresponding K values (K_{High}, K_{Fill}, K_{Low}) vary over 3 orders of magnitude, but are equivalent in volumetric proportion. To make the truncated Gaussian and facies fields comparable, the global geometric mean and variance of ln(K) are identical across models (see Table 2). The truncated Gaussian model is identical to a Gaussian model except that values of K larger than K_{High} or lower than K_{Low} are "truncated" or set equivalent to K_{High} or K_{Low}, respectively (see Figure 2). The truncated Gaussian model is chosen in this analysis over the Gaussian one because extreme values of K are better connected in truncated
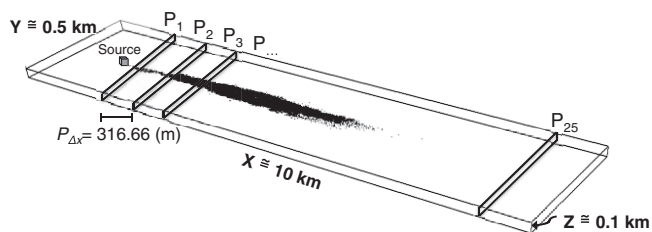

Figure 1. Schematic of the simulation flow domain, showing location of instantaneous source with respect to the twenty-five planes (P1-P25) where BTCs are obtained. Note: figure is not to scale.

Table 2. Heterogeneity Parameters

Anisotropy Ratio	Value	Units
$\varepsilon_1 = 0.1$ (-)	$I_x = 15.0$	(m)
$\varepsilon_4 = 0.0125$ (-)	$I_x = 120.0$	(m)
$\varepsilon_7 = 0.0015625$ (-)	$I_x = 960.0$	(m)
*For all scenarios	$I_y = 15.0, I_z = 1.5$	(m), (m)

Parameter	Value	Units
Geometric mean of K	$K_G = 1.0$	(m d^{-1})
Variance of ln(K)	$\sigma^2 = 5.29$	(-)
Facies K values	$K_H = 10.0, P_H = 0.33$	(m d^{-1}), (-)
and proportions	$K_F = 1.0, P_F = 0.34$	(m d^{-1}), (-)
	$K_L = 0.1, P_L = 0.33$	(m d^{-1}), (-)
Facies off-diagonal transition probabilities (all directions)	$r_{HL} = r_{LH} = 0.5$	(-)

Gaussian fields. Therefore, BTCs resulting from the truncated Gaussian model more closely resemble facies model BTCs, making the comparison with the facies model less biased.

2.2. Sensitivity to Statistical Anisotropy and Local Dispersivity

Autocorrelation of K is defined in the x, y, and z directions via the integral scale: I_x (m), I_y (m), I_z (m). Statistical anisotropy of K is defined via the ratio: $\varepsilon = I_z/I_x$ (-). The effect of statistical anisotropy is analyzed by varying the magnitude of I_x, ranging from 15.0 (m) to 960.0 (m), while the magnitudes of I_y and I_z are held constant (see Table 2). For both the truncated Gaussian and facies cases, three ε cases are used from *Siirila-Woodburn and Maxwell* [2015], ranging from least anisotropic (ε_1), intermediate anisotropic (ε_4), and most anisotropic (ε_7) (see Table 2).

Because we are interested in the behavior of individual BTCs and not ensemble statistics, our methodology does not utilize any spatial or temporal averaging across realizations. That is, for each combination of heterogeneity model (TG, F) and anisotropy ratio (ε_1, ε_4, ε_7), BTCs at each of the 25 down-gradient planes are compared independently. To ensure that the chosen realization is of "typical" behavior within the ensemble, two additional realizations from each combination of heterogeneity model/anisotropy ratio are chosen randomly to compare for similarities or differences. This precaution is only necessary given flow field global statistics that yield greater variance in BTCs across realizations. From the results of *Siirila-Woodburn and Maxwell* [2015], ensembles with a small variance in comparative metrics are those in the facies model, and with the least anisotropy (ε_1) whereas ensembles with a high variance are those in the truncated Gaussian model, and with the highest degree of anisotropy (ε_7).

We are also interested in BTC sensitivity to local dispersivity, as it may play an important role in BTC shape via induced solute mixing at smaller scales. As molecular diffusion is typically 1 or more orders of magnitude smaller than the effects of mechanical dispersion, except in the case of very slow groundwater velocities [e.g., *Cherry et al.*, 1984], the effect of molecular diffusion is assumed small in this analysis, and we combine diffusion and dispersion with an "effective" dispersivity value. We define the inclusion of local dispersion in our simulations through the dimensionless Peclet number, $Pe = I_x/\alpha_L$ (-), where α_L is longitudinal dispersivity (m). For all scenarios, transverse dispersivity, α_T (m), is equivalent to $0.1(\alpha_L)$. All heterogeneity model-anisotropy combinations are simulated with four cases of local dispersivity, where α_L vary over 3 orders of magnitude, and where Pe numbers range from 9.6×10^5 (-) to 1.5×10^2 (-) (see Table 3). One infinite (I) and three discrete (D1–D3) cases of Pe are simulated with the following α_L and α_T values:

Case I: $\alpha_L = \alpha_T = 0.0$ (m), equivalent to $Pe = \infty$

Case D1: $\alpha_L = 0.001$ (m); $\alpha_T = 0.0001$ (m)

Case D2: $\alpha_L = 0.01$ (m); $\alpha_T = 0.001$ (m)

Case D3: $\alpha_L = 0.1$ (m); $\alpha_T = 0.01$ (m)

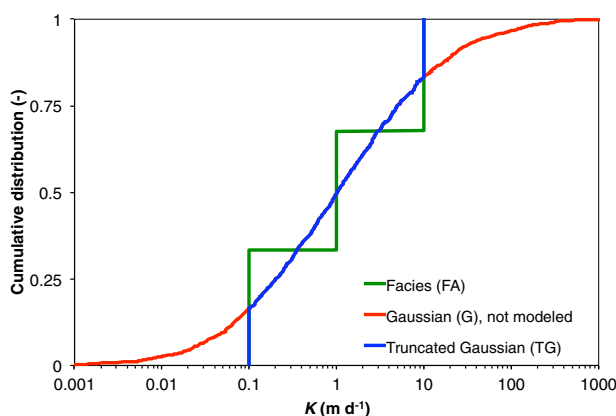## 2.3. BTC Reconstruction to Assess Transport Connectivity and Local Peaks

A total of 1,800 BTCs are assessed for transport connectivity and local peaks, corresponding to each of the 25 planes with varying heterogeneity model (TG, F), anisotropy ratios (ε_1, ε_4, ε_7), Pe (4 scenarios), and

Figure 2. Distribution of hydraulic conductivity, K, for the two heterogeneity models used in this study (modified from Siirila-Woodburn and Maxwell [2015]).

Table 3. Pe (-) Given Varying Anisotropy Ratios and Local Dispersivity Cases

	$\varepsilon_1 = 0.1$ (-)	$\varepsilon_4 = 0.0125$ (-)	$\varepsilon_7 = 0.0015625$ (-)
Case I	$Pe = \infty$	$Pe = \infty$	$Pe = \infty$
Case D1	$Pe = 1.5 \times 10^4$	$Pe = 1.2 \times 10^5$	$Pe = 9.6 \times 10^5$
Case D2	$Pe = 1.5 \times 10^3$	$Pe = 1.2 \times 10^4$	$Pe = 9.6 \times 10^4$
Case D3	$Pe = 1.5 \times 10^2$	$Pe = 1.2 \times 10^3$	$Pe = 9.6 \times 10^3$

realizations (3). Although more formally defined below in section 2.3.2, a "local peak" is considered as any fluctuation in the BTC changing locally from a positive to negative slope (i.e., from a rising limb to falling limb).

The challenge when looking at such local details is to ensure that peaks and slopes are a real outcome of the system rather than a numerical artifact. To this end, we avoid the use of Eulerian methods to prevent oversmoothing caused by the need to use low Pe numbers. Thus, a fully Lagrangian method was used. To avoid artificial fluctuations in the solute BTC caused by the finite number of particles used, we combined a large number of particles ($np = 400,000$) with a locally adaptive optimal kernel density estimator (KDE). Optimal KDE methods have been recently proposed in the particle tracking literature to overcome oversmoothing and artificial fluctuations caused by the use of a limited number of particles [*Fernàndez-Garcia and Sanchez-Vila*, 2011; *Pedretti and Fernàndez-Garcia*, 2013]. The basis of the KDE approach used in our work is the universal adaptive bandwidth (UAB) method developed by *Pedretti and Fernàndez-Garcia* [2013]. UAB is automatic, and locally adaptive, playing on the strengths of the established global and adaptive bandwidth methods especially to reconstruct heavy-tailed BTCs. Following *Pedretti and Fernàndez-Garcia* [2013], the singular input parameter which controls sensitivity, α, is specified as 0.5 (-) (α values must range from [0, 1]). Remarkably, at this stage it is important to highlight that KDE methods also provide a scientific basis to quantify the size of artificial fluctuations in particle tracking solutions, which is a key aspect to consider in identifying local peaks.

Sensitivity to the use of the KDE and the number of particles is assessed to avoid artificial effects on the BTC shape. In reality, the true BTC will only be achieved in the limit (i.e., an infinite number of particles), as oscillations in BTC error decrease inversely with $np^{1/2}$. To select the number of particles to be used, preliminary simulations involving different quantities of particles were conducted (np varying over 3 orders of magnitude, see Figure 3). As np increases from 4,000 to 40,000 to 400,000 particles (red, green, and blue points, respectively), the shape of the BTC becomes more defined. Curves reconstructed from 40,000 and 400,000 are almost identical in shape and in the number of local peaks displayed, except for very late times corresponding to low concentrations (i.e., where few particles are passing the plane).

From this preliminary analysis, and taking a conservative methodology, 400,000 particles were selected for all simulations. Analysis of local peaks and corresponding slopes is conducted from KDE reconstructed breakthrough curves. We stress the necessity of using the KDE for BTC reconstruction as even though trends in shapes may be visually evident from the particle tracking raw BTCs (e.g., blue points in Figure 3), quantitatively assessing the number of local peaks via changes in slope direction was infeasible due to erraticism in the raw particle tracking signal. Lastly, confidence intervals in the KDE were also calculated as a function of np. As described in more detail in Appendix A, the 95% confidence interval is very small, always smaller than about 10^{-7} for 400,000 particles, where the coefficient of variation for even very jagged BTCs is less than 5% except during very late times when the number of particles passing the plane is very low. Thus, the effect of the KDE and number of particles is considered negligible, and any oscillations in the BTCs are considered resulting from the heterogeneous flow field and are not biased due to the methods used.
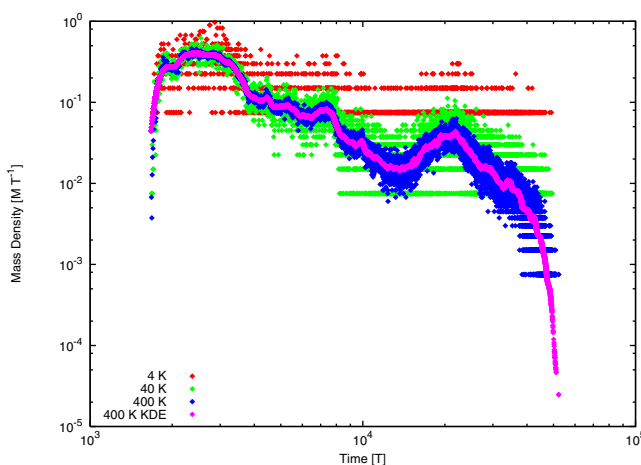

Figure 3. Example particle tracking breakthrough curve simulated with varying numbers of particles (red, green, and blue points) and the corresponding kernel density estimator (KDE) reconstructed breakthrough curve for the 400,000 particle simulation (pink points).

2.3.1. Calculation of Transport Connectivity

From the KDE reconstructed BTC, we obtain the transport connectivity indicator $CI = t_{50}/t_5$ (-), where t_{50} (y) and t_5 (y) are the times at which 50% and 5% of the plume mass pass the plane, respectively [*Knudby and Carrera*, 2005]. Given that the CI metric assesses the shape of the BTC, it is used to quantify channeling through preferential flow pathways. A higher CI value signifies a BTC skewed towards earlier arrival times, and most often display significant tailing.

2.3.2. Classification of Local Peaks

Next, from the KDE reconstructed BTC local peaks are found and classified according to the duration in which the slope of the BTC remains negative. Recall that for each realization a BTC is obtained at each of the 25 observation planes. From each log-log curve, we define the time-dependent variable, slope, $s(t) = d\log(m)/d\log(t)$, where m [$M\,T^{-1}$] is mass discharge and t [T] is time. From the sign of s, we can determine the presence of a local peak. The duration of a local peak coincides with the duration of when the derivative changes from positive to negative (i.e., from a local maximum in the BTC to the following local minimum, or from a rising to a falling limb). For the purpose of discussion, we disregard all local peaks with a duration smaller than 20 simulation time steps. Local peaks with a duration ranging between 20 and 100 time steps are denoted as "significant local peaks, SLPs," and those extending over 100 time steps as "major local peaks, MLPs." This distinction is illustrated in Figure 4a. These cutoff points were found to be suitable in distinguishing local peaks in our simulations, but are not to be interpreted as absolute endpoints for all BTCs. Visual inspection was first used to determine such cutoff points. First, the major cutoff was found by ensuring all BTCs contain at least one major peak (notice that standard BTCs would display one single peak that would then be considered major). Second, the significant cutoff was found by distinguishing significant peaks from those which are and are not visually apparent in the BTC, and which are greater than the 95% confidence interval of the KDE (see Appendix A). Naturally, this procedure will be data specific, and will vary given the time step and duration of the BTC. This procedure is not intended as strict guidelines to determine differences in BTC peaks, but rather to allow for quantitative inspection of the BTC and discussion of BTC shape and evolution with travel distance. Although local peaks are defined here with regard to their duration, other methodologies similar to the above could be conducted with regards to the magnitude in mass. Additionally, it is important to note that although the definition of a local peak here is with regards to time, the methodology used does not disregard the importance of the magnitude in mass as part of defining local peaks. Given that significant and major peaks are ensured to be greater than the 95% confidence interval of the KDE, in essence local peaks are also defined here with regards to their magnitude. With this, it is statistically guaranteed that significant and major peaks are associated with real oscillations in the BTC caused by heterogeneity, and are not errors associated with the methods used or the presence of a finite number of particles.

2.4. Determination of Slopes

Using this methodology, slopes for significant and major local peaks are analyzed. Determining the slope of a BTC is done by the incremental ratio, and thus requires a proper method to assess the length of the curve that will be used to estimate the slope (see definition and discussion by *Willmann et al.* [2008]). As shown in Figures 4b and 4c, for an individual local peak, the portion of the BTC of interest starts from the initial point at which the slope changes from positive to negative (t_i), and extends to the final point at which the slope retains a negative value (t_f). However, as the signal between these two points may vary in the degree of noisiness, a final cutout point in the local peak prior to t_f may need to be defined. In doing so, the tail end of the slope is not over sampled, which may add a bias in the determination of the slope. For example, a scenario which this extra precaution is necessary if the slope changes very drastically as t approaches t_f, and the final portion of the local peak is not be representative of the overall local peak slope, warranting exclusion from the calculation. The determination of the cutoff point, t_{sample} is described in Appendix B.

3. Results and Discussion

3.1. Evaluation of Transport Connectivity

Figure 5 shows CI (-) results as a function of dimensionless travel distance, DI_x^{-1} (-), where D (m) is the x direction travel distance from the source to the plane and I_x varies depending on statistical anisotropy, ε. Physically, DI_x^{-1} can also be thought of as the number of integral scales traveled. CI is shown in different
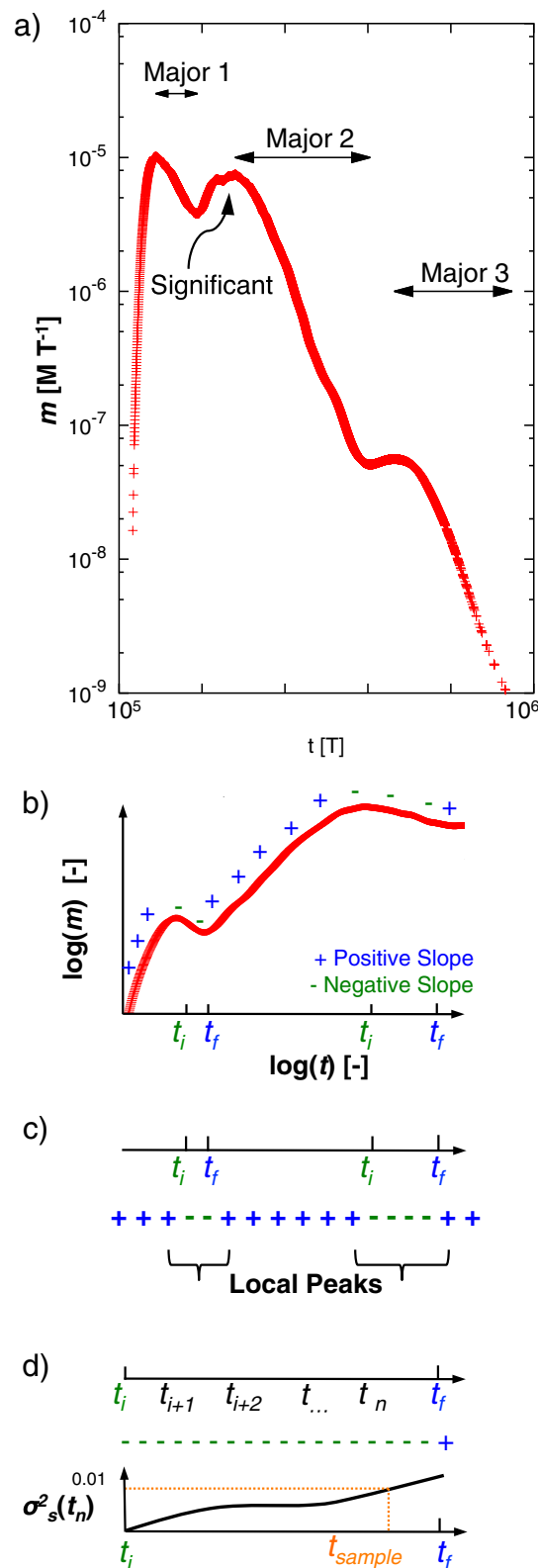
Figure 4. a) Example kernel density estimator reconstructed breakthrough curve determined to have one significant and three major peaks. b) Determination of t_i and t_f for each local peak based on changes in slope sign. c) Definition of local peaks given changes in slope sign. d) Determination of local peak slope at the time tsample, with the use of a cutoff point in variance, σ^2_s, t.

subplots for the four cases of local dispersion (rows, Figure 5) and heterogeneity models (columns, Figure 5). Differences in ε are denoted by color (see key in subplot a) for three representative realizations each. As described in section 2.3.1, a high CI value corresponds to high preferential flow favoring anomalous transport; low values are indicative of more Fickian transport.

3.1.1. Effect of Anisotropy on Transport Connectivity, CI

Two generalities can be made: (1) as the number of integral scales traveled increases, CI decreases and (2) greater anisotropy cases (ε_7) result in greater initial CI values compared to more isotropic cases (ε_1). An exception exists for the TG-ε_7-ε_4 scenario (Figure 5, left column), discussed below. CI is also much more variable within the first 10 integral scales traveled, suggesting that early transport flow paths are also more variable during this time. These results are expected, as it is logical that the probability of a fast flow path existing between the source and plane after short travel distances is high and vice versa (where the probability of connected flow paths after long travel distances is low). What is interesting to note is that at the smallest dimensionless travel distance (DI_x^{-1}), the ε_1 CI value is slightly larger than the ε_4 CI value. Similarly, at this short travel distance the ε_4 CI value is slightly larger than the ε_7 CI value. This implies that if considering true travel distance (D), transport connectivity is slightly greater for more anisotropic aquifers. This is consistent with previous analyses exemplifying the importance of statistical anisotropy in both dimensional and dimensionless space [*Siirila-Woodburn and Maxwell*, 2015] but differs from the work of *Zarlenga et al.* [2013] which found a weak dependence of ε on BTC results for any degree of the spatial heterogeneity of the porous formation. Some key differences in numerical setups between this analysis and *Zarlenga et al.* [2013] should be noted, primarily that the ε in our analysis range over a much greater parameter space. The most anisotropic aquifer in this analysis is approximately 65 times more anisotropic of that of *Zarlenga et al.*; in fact, the lowest ε of *Zarlenga et al.* is equivalent to the highest statistical anisotropy ratio in this study ($\varepsilon_1 = 0.1$).

3.1.2. Effect of Heterogeneity Model on Transport Connectivity, CI

In general, the truncated Gaussian model generates random fields with well-connected heterogeneous structures that can distribute solutes in relatively fast channels. This effect is more
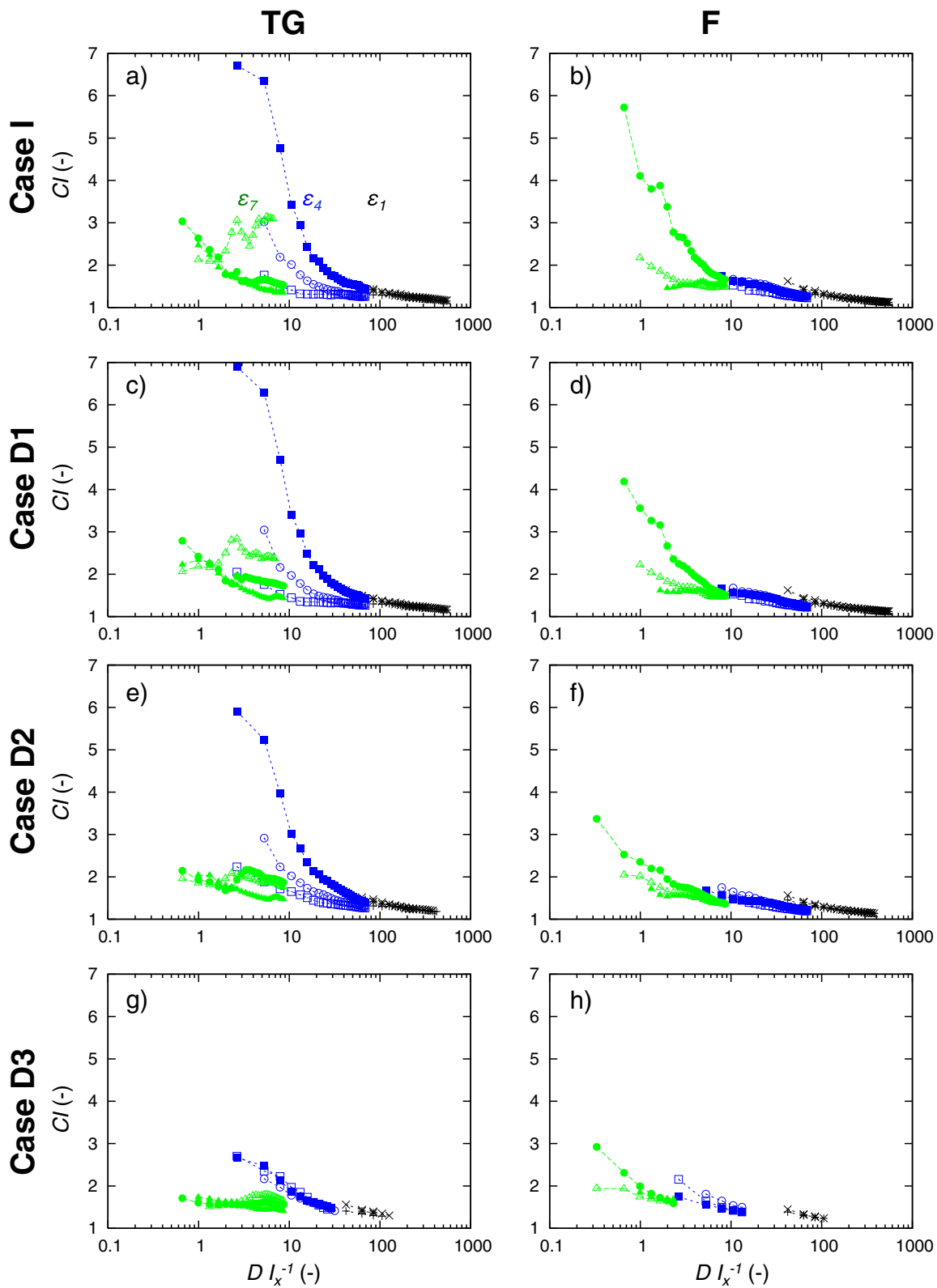
Figure 5. Transport connectivity index as a function of dimensionless travel distance for different cases of local dispersivity (rows) and heterogeneity models (columns). Statistical anisotropy cases are distinguished by color (ε_1, ε_4, ε_7; see sub-plot a) for three realizations each (denoted by different symbols).

apparent for large Pe numbers (advective dominated problems, discussed in the following section) and intermediate anisotropy ratios. Again while generally the CI increase as the number of integral scales traveled increases, an exception persists for the TG-ε_7-ε_4 scenario (approximately between 5 and 10 dimensionless travel distances, DI_x^{-1}). Here ε_4 realizations yield CI values higher than those of ε_7 realizations. To explain this effect, we first need to recognize that even though both heterogeneity models share the same global statistics, they are quite different in nature. The facies model describes a categorical variable that can take a fixed number of values whereas the truncated Gaussian model, instead, represents a spatially continuous random process defined over a wide range of possible values. Consequently, the facies model assigns a predefined average value of K in each facies, whereas the truncated Gaussian model accounts for heterogeneity within a larger range of K values. It is likely that these differences make the general CI trends more clear for the facies model than the truncated Gaussian model.

3.1.3. Effect of Local Dispersion on Transport Connectivity, CI
In general, as the magnitude of local dispersivity increases (rows in Figure 5) CI also decreases, and the effects of heterogeneity are diminished. Differences between anisotropy, ε, also decrease. Essentially, the increases in local dispersion (especially in the transverse direction) produce a better mixed solute system, causing the particles to jump from areas of high transport conductivity (fast channels) to areas of low transport conductivity (areas with relatively low groundwater velocities) and thereby a faster homogenization of the entire system.

3.2. Evaluation of Local Peak Statistics
Figures 6 and 7 show the local peak statistics for major and significant local peaks, respectively. Again, results are shown as a function of dimensionless travel distance, DI_x^{-1}. Local peaks are shown in different subplots for the four cases of local dispersion (rows) and heterogeneity models (columns). Differences in ε are denoted by color (see key in subplot a).

3.2.1. Trends in Statistics and Conceptual Model of the Physical Mechanism Causing Local Peaks
The number of significant local peaks (Figure 7) is in some scenarios 2 or 3 times greater than the number of major local peaks (Figure 6) (note that the y axis frequency range is different in both plots to accommodate for such differences). This result was expected, as it is inherent in our definition of local peaks (section 2.4) to favor a smaller number of major local peaks than significant local peaks. It is interesting to note that for some cases (e.g., TG, Case I, ε_7) the number of major local peaks is as high as 20 (Figure 6a) and the number of significant local peaks is as high as 50 (Figure 7a), suggesting very jagged BTCs. In contrast, most of the ε_1 scenarios yield very smooth BTCs, where statistics show only one major local peak, and very few or zero significant local peaks. The latter would indicate more traditional definitions of BTCs and more Fickian-like transport, where solute particles are normally displaced around the centroid of the plume [e.g., *Rubin*, 2003], whereas the former is not easily mathematically defined.

As mentioned in section 1, bimodal BTCs have been observed due to dual-domain permeability fields, fracture flow, or kinetic sorption. Here we demonstrate that heterogeneous flow fields of both continuous and discrete K distributions can result in multipeak BTCs. These statistically based results are of the first to characterize multipeak BTC behavior in three-dimensional porous media, and demonstrate (1) the ability to quantify localized peaks of different magnitudes as a function of travel distance, (2) the array of local peak frequencies given differences in hydrogeologic parameters and models, and (3) the ability to determine physical mechanisms controlling the shape of the BTC, as discussed in the following sections.

From these results, a few trends are notable. First, the number of local peaks (both major local peaks and significant local peaks) varies as a function of dimensionless travel distance, DI_x^{-1}. In general, the highest number of local peaks occurs at an intermediate DI_x^{-1} respective to each ε; an explanation why is discussed below. Then within a given anisotropy ratio, ε, the number of local peaks diminishes as DI_x^{-1} increases, so that the number of significant local peaks decreases towards zero, while the number of major local peaks trends towards one or two (Figure 6). The question is what is the physical mechanism creating these local peaks? Furthermore, why do significant and major peaks behave differently?

Conceptually, we propose these peaks are created by preferential flow in the aquifer, and that the degree of preferential flow (as shown in section 3.1) is correlated to the degree which the aquifer has been sampled. The conceptual model includes two types of travel pathways. Smaller peaks in the breakthrough curve result from smaller parcels of solutes traveling either quicker or slower than the bulk of the solute
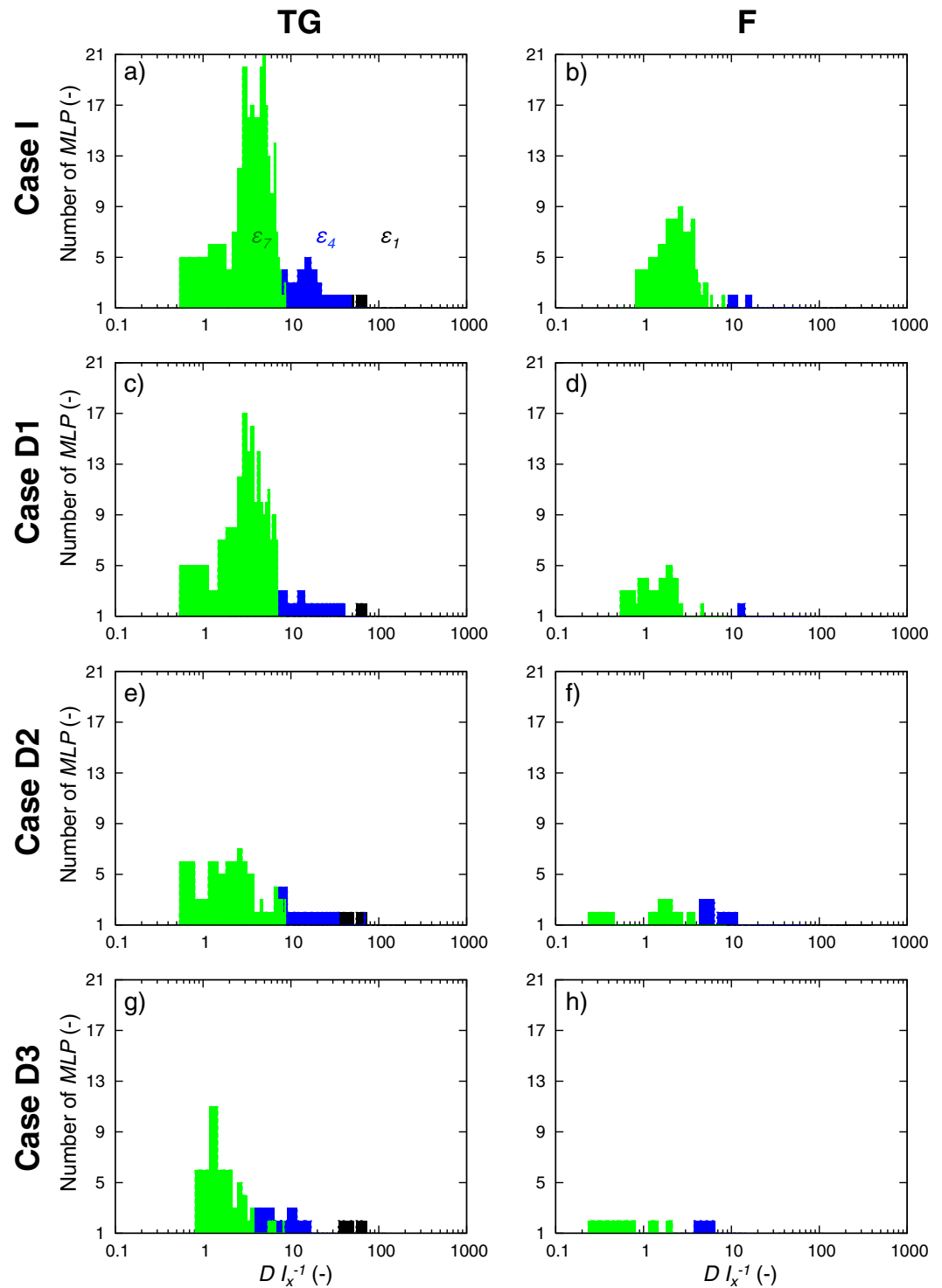
Figure 6. Major local peaks statistics as a function of dimensionless travel distance for different cases of local dispersivity (rows) and heterogeneity models (columns). Statistical anisotropy is shown by color (ε_1, ε_4, ε_7; see sub-plot a). Note that since all BTCs have at least one MLP, the y-axis begins at a value of unity to illustrate those BTCs that have more than one MLP.

(i.e., via aquifer channeling through high K material or diffusion out of low K material). Major peaks are formed from the bulk of the solute moving at the mean groundwater velocity, and resulting in fewer and longer duration peaks in the breakthrough curve. As the number of integral scales traveled increases, a few dynamics may be occurring. First, as more of the aquifer is sampled, the probability of small, fast, or slow
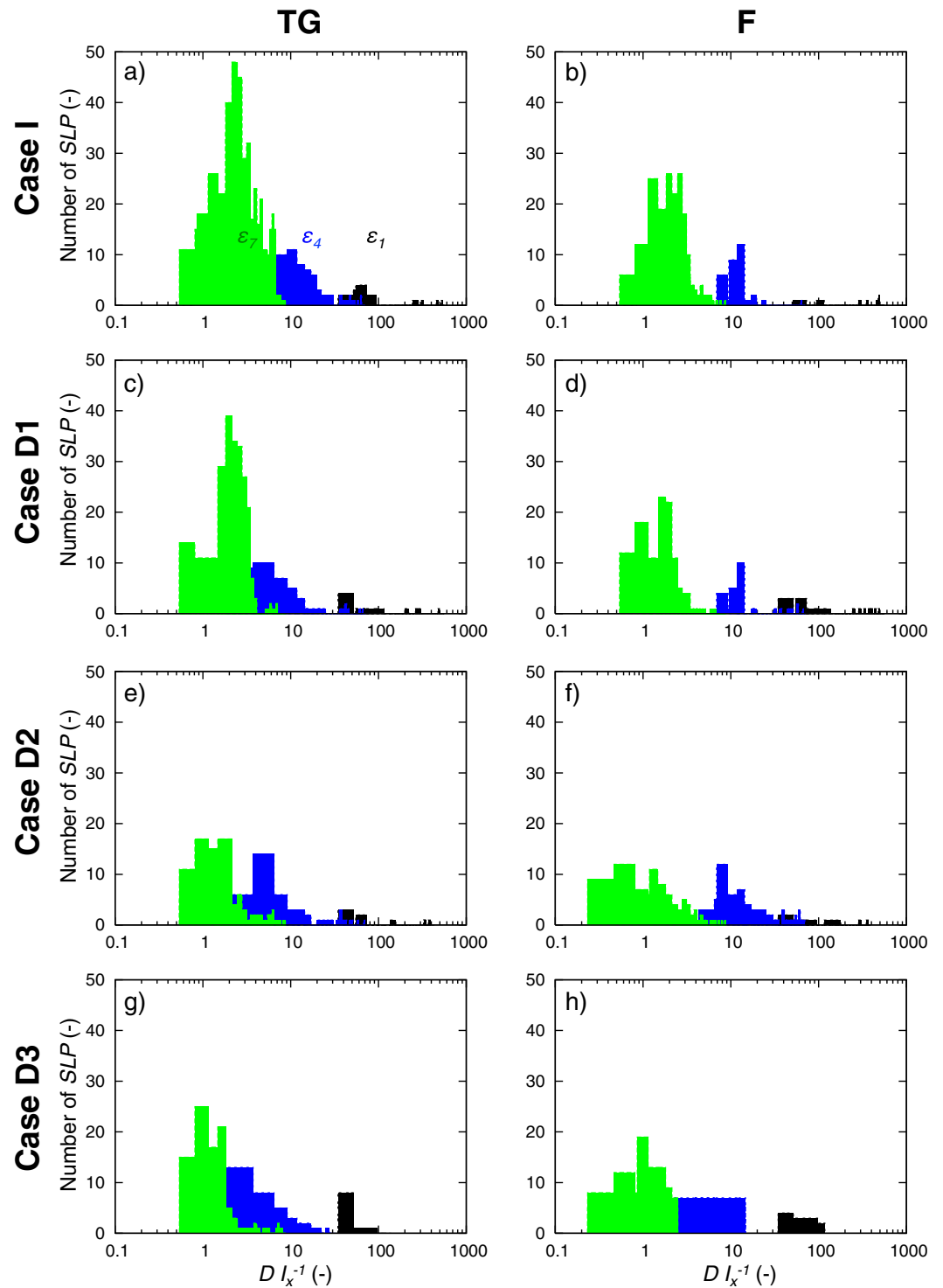
Figure 7. Significant local peaks statistics as a function of dimensionless travel distance for different cases of local dispersivity (rows) and heterogeneity models (columns). Statistical anisotropy is shown by color (ε_1, ε_4, ε_7; see sub-plot a).

travel pathways between the source and the plane decreases. Secondly, dynamics related to aquifer sampling are also occurring; as solute parcels encounters both high and low K regions of the aquifer, the travel times between different localized parcels become more similar, thus the occurrence of distinct localized peaks decreases. This behavior is consistent with the BTC approaching a singular, monopeak curve. After even more sampling of the aquifer is completed, a Fickian regime is then approached. Our statistical trends

in local peak results quantitatively show agreement with this conceptual model. We attribute the number of significant local peaks tending toward zero as localized pathways in the aquifer ending or being dispersed into the bulk movement of the solute, and the number of major local peaks tending towards a small finite number of peaks (either singular or double peak depending mainly on ε) as localized pathways mixing with the bulk of the solute plume.

Although the disappearance of significant local peaks and rise to a finite number of major local peaks indicates the Fickian regime is being approached, the true Gaussian setting time where purely Fickian behavior is observed may not be reached at this point. One way to assess such properties is by means of moment analysis [*Zhang and Meerschaert*, 2011] or metrics such as the dilution index, which indicates when plumes are well mixed or display pockets of high concentrations [*Kitanidis*, 1994; *Trefry et al.*, 2003]. We define the convergence of the BTC shape to a singular major peak as the "mono-peak regime," a classification which precedes the true Fickian regime. Our conceptual model is consistent with that of other numerical simulations which report non-Fickian particle displacement due to opposing sequestration and channeling effects [*Trefry et al.*, 2003; *Zhang et al.*, 2013].

To illustrate this conceptual model further, Figure 8a shows an example BTC with a clear bimodal major local peak BTC. The spatial locations of particle breakthrough at the measurement plane are also shown at 2 times corresponding to the bimodal peak breakthrough in Figures 8b and 8c. The highest concentration of particle breakthrough locations differs between the first and second major local peak (i.e., in Figure 8b the highest particle concentration is centered near Y = 285 (m), Z = 45 (m), whereas in Figure 8c the highest particle concentration is centered near Y = 275 (m), Z = 52 (m). From this illustration, we can infer that a plausible mechanism for the bimodality of the BTC in the example is that a portion of the plume has been physically rerouted in the aquifer; otherwise, the breakthrough of both peaks would occur at the same spatial location in the measurement plane. Physical rerouting occurs when contrasts in the K field lead to shearing of the plume. A simplified schematic of a plume before and after a shearing event is shown in Figures 9a and 9b, respectively. These individual shearing events lead to different solutes routes, and ultimately appear as individual peaks in the BTC. Initially, the number of local peaks in the BTC is driven by the number of different velocity pathways connecting the source to the plane; for a Gaussian model this number will be greater than that resulting from a discrete facies model. Assuming the source samples all facies types, and without any local dispersion, the number of major local peaks in a facies simulation at short travel distances will be equivalent to the number of K values present (see Figure 6b). For both models, as the bulk of the plume has traveled some distance, shearing events occur, effectively dividing portions of the plume. After long travel distances, the plume has been separated by these shearing events, making the shearing of a large, concentrated parcel less probable. This is why the highest amount of significant and major local peaks occurs at intermediate travel distances (Figures 6 and 7). In the following sections (sections 3.2.2–3.2.4), the effects of hydrogeologic modeling parameters (anisotropy, heterogeneity model, and local dispersion, respectively) which affect preferential flow and the conceptual model explaining how a local peak is formed, are quantitatively assessed.

3.2.2. Effect of Anisotropy on Local Peak Statistics

For both major local peaks and significant local peaks, the frequency of local peaks is very sensitive to anisotropy. Specifically, the larger the statistical anisotropy (ε_7) the greater the frequency of local peaks (both major local peaks and significant local peaks). Because statistical anisotropy has been linked to the concept of aquifer connectivity [*Siirila and Maxwell*, 2012a, 2012b; *Siirila et al.*, 2012; *Navarre-Sitchler et al.*, 2013], we hypothesize that this effect is linked to the concept of preferential flow (see Figure 5). Our results show that more isotropic aquifers are unlikely to result in BTCs with more than one major local peak, regardless of heterogeneity model or local dispersivity. As more integral scales have been traveled, most ε_1 BTCs will contain only one major local peak and very few or zero significant local peaks. In contrast, highly anisotropic aquifers result in BTCs which are very non-Gaussian, often characterized by 5–20 major local peaks and up to 50 significant local peaks. To illustrate this further, Figure 10a shows three BTCs at the same arrival plane (plane 9 in this case), produced with the truncated Gaussian model. In this example, the most anisotropic case yields a very noisy BTC with multiple major local peak and significant local peaks, whereas the least anisotropic case produces a singular major local peak and zero significant local peaks. Of intermittent BTC noisiness is the intermediate anisotropy ratio, showing a clear bimodal major local peak and one significant local
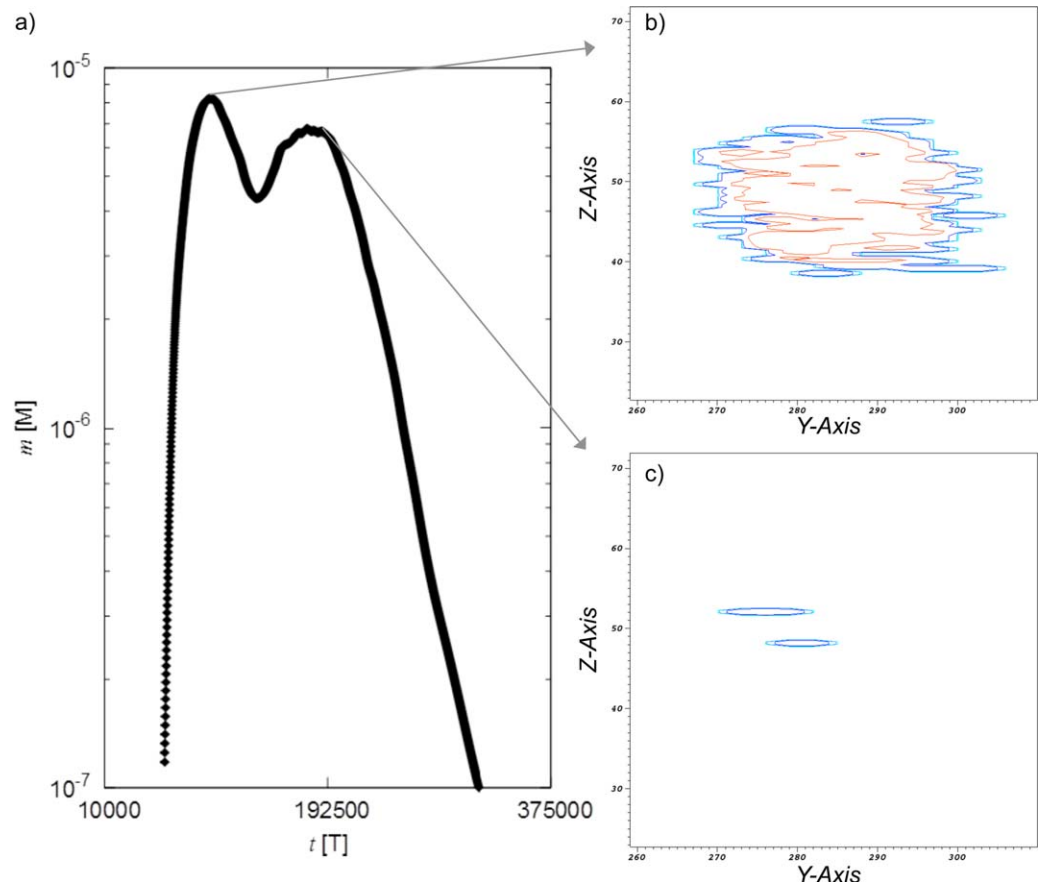
Figure 8. a) Example breakthrough curve and b-c) corresponding particle breakthrough locations in the plane orthogonal to the x-axis at two snapshots in time (dictated by arrows). The highest concentration of particles passes the plane at different spatial locations at these local peaks (i.e. in Figure 8b the highest particle concentration is centered near Y = 285 m, Z = 45 m, whereas in Figure 8 c the highest particle concentration is centered near Y = 275 m, Z = 52 m), exemplifying the concept of preferential flow being the main mechanism causing the occurrence of local peaks in the breakthrough curve.
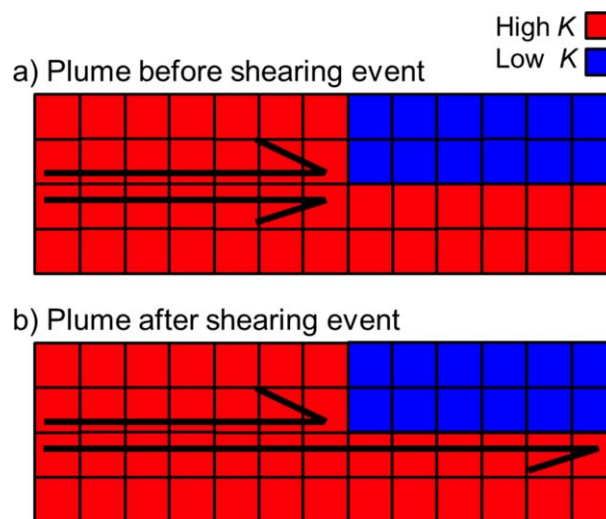

Figure 9. Schematic illustration of plume shearing due to contrasts in K in the direction of mean flow.

peak. Although the numbers vary with the choices of heterogeneity model and local dispersion cases, statistical anisotropy of K is a key parameter in determining the BTC shape.

The number of integral scales required to reach the aforementioned monopeak regime varies with ε. For example, in some cases after 10 integral scales have been traveled, the monopeak regime is approached in the most anisotropic cases (ε_7) but not in the intermediate anisotropy case (ε_4). This result is contrary to the results of many earlier studies, which typically only consider the Gaussian setting time from the evolution of plume spreading as a function of dimensionless travel distance, and without considering the presence of multiple peaks. For example, the number of
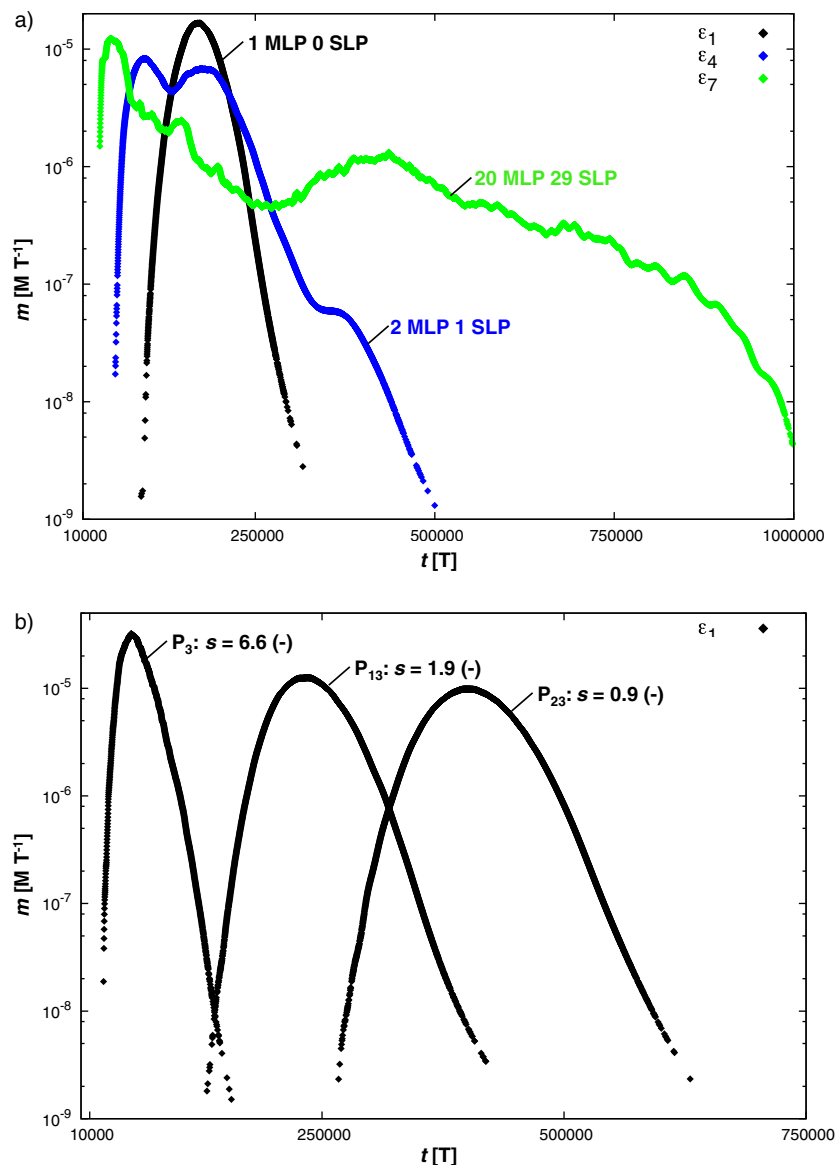
Figure 10. a) Example breakthrough curves in semi-log space showing differences in the number of major and significant local peaks (MLP and SLP, respectively). For the three anisotropy ratios (see colors key), each breakthrough curve is at the same travel distance (i.e. P9 in this example). b) Example evolution of a mono-major local peak breakthrough curve as a function of travel distance. The curve shown is the same produced from the ε_1 field as in a) for planes 3, 13 and 23. Corresponding slopes, s, are also noted.

integral scales needed to reach the Fickian regime is typically thought to be on the order of several hundreds of integral scales [*Trefry et al.*, 2003; *Zhang and Meerschaert*, 2011; *Zhang et al.*, 2013], regardless of anisotropy. *Dagan* [1988] showed that compared to more isotropic media, the longitudinal macrodispersion asymptote for highly anisotropic media is reached after fewer integral scales traveled, although the difference was very small. In fact, our simulations show the opposite; more integral scales are required to reach a monopeak regime for more anisotropic aquifer. A possible hypothesis for this phenomenon is that over the same dimensionless travel distance, in more anisotropic media there is more preferential flow, less plume mixing, and less parcels of the plume converging, thus leading to more peaks in the BTC when compared to more isotropic media.

As the number of integral scales traveled for each ε scenario differs, it is difficult to decipher how sensitive reaching this regime is to ε. Regardless, because the overall trends in major local peaks and significant local peaks are similar within each ε, importance may be stressed on BTC shape with regards to true travel distance, D, opposed to dimensional travel distance, DI_x^{-1}. That is, while anisotropy may be important in
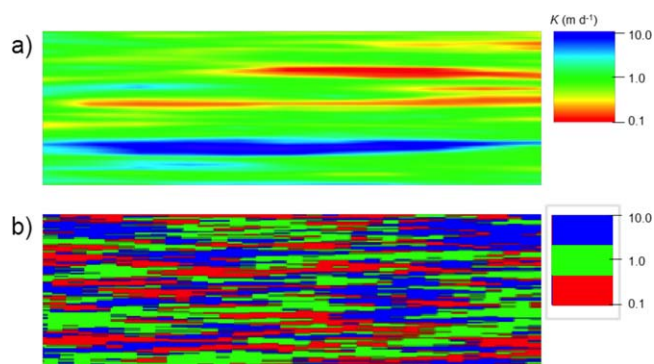
Figure 11. Example cross-sections showing isolation of high and low *K* values in TG fields (a) and adjacency of high and low *K* values in F fields (b).

determining the number of local peaks, the travel distance required to reach the monopeak and Fickian regimes is not necessarily proportional to the magnitude of the integral scale.

3.2.3. Effect of Heterogeneity Model on Local Peak Statistics
The effect of heterogeneity model selection has a large impact on the frequency of local peaks. The truncated Gaussian models result in a larger number of major local peaks and significant local peaks as compared to the facies model results

(Figures 6 and 7, left versus right column, respectively). Following section 3.1, we see that the lack of strong transport connectivity resulting from the zonal representation of the ln(*K*) field in the facies model (Figures 6 and 7) results in a reduction of the frequency of peaks in the facies model. This is consistent with the model comparison results of *Siirila-Woodburn and Maxwell* [2015], which show that there is more uncertainty in transport metrics for the truncated Gaussian model, a possible indication of more variability in the BTC.

It is also important to note that while the distribution of *K* in these models is similar, they are not exact (see Figure 2). The intermediate values of *K* in the truncated Gaussian model, i.e., $K > 0.1$ and < 1.0 (m d^{-1}) or $K > 1.0$ and < 10.0 (m d^{-1}), are likely responsible for the differences in truncated Gaussian and facies plume behavior. For example, our results show that facies models result in smoother BTCs compared to truncated Gaussian models. Due to the discrete nature of the *K* field in the facies model, resulting plumes are likely affected by two mechanisms: (1) a smaller number of concentrated, localized pathways in the flow field and (2) the range and combination of local velocities are much fewer in number when compared to the truncated Gaussian model (see plume snap-shots in Figure 6 of Siirila-Woodburn and Maxwell [2015]). Lastly, recall that Gaussian models result in smoothly varying spatial changes in *K*, resulting in areas of spatially isolated high or low *K* materials, whereas facies models may result in adjacent high or low *K* materials (depending on the statistics and transition probabilities). This pattern is visually evident from cross sections of representative realizations, as shown in Figure 11. This difference could affect aquifer connectivity (see Figure 5), where early breakthrough in the facies model is dictated primarily by the K_H facies and late breakthrough is dictated primarily by the K_L facies. In contrast, flow in the truncated Gaussian model is dictated by a range of *K* values. With this in mind, it is logical that there are less major local peaks and significant local peaks in the facies model, where even if localized pathways exist, they are primarily driven by only two discrete values of *K*: K_H and K_L.

3.2.4. Effect of Local Dispersion on Local Peak Statistics
In general, as the magnitude of local dispersivity increases (rows in Figures 6 and 7), the number of both major local peaks and significant local peaks decrease. The exception to this trend is the highest level of local dispersivity, Case D3, for significant local peaks (Figures 7g and 7h) and for the truncated Gaussian major local peak case (Figure 6g), as discussed below. Few studies have assessed the impact of local dispersivity on the shape of the BTC, but theoretically local dispersivity should add additional solute mixing, as it is usually implemented in transport modeling to account for local or subgrid heterogeneity [*Rubin et al.*, 1999].

This theoretical behavior is consistent with results for finite *Pe* (Case I), and high *Pe* numbers simulated (Case D1 and Case D2, see Table 3). As shown here, as local dispersivity is increased, the number of major local peaks and significant local peaks decreases. For the lowest *Pe* numbers simulated (Case D3, see Table 3), we actually see an increase in both major local peaks and significant local peaks (Figures 5g, 6g, and 6h). This increase is potentially due to solutes jumping from areas of high *K* to areas of low *K*, and vice versa. Our results show that a certain amount of local dispersivity increases aquifer sampling, causing a homogenization effect of the plume, and thus the occurrence of less individualized peaks in the BTC. At a higher

amount of dispersivity, however, a threshold is reached where sampling of the aquifer increases to include very fast or very slow pathways. As a result, more potential shearing events and thus more complex shaped plumes BTCs are observed.

Major local peaks for the facies model, Case D3 (Figure 6h) are insensitive to the increase in local dispersion, potentially because at this level of aquifer mixing, particles jumping between the three facies types does not greatly affect the bulk of the plume, but rather smaller pathways and hence the number of significant local peaks (Figure 7h). Although local dispersion is often neglected, the importance of particle jumps due to local dispersion (especially in the transverse direction) has been noted recently, where plume retardation or acceleration in anisotropic aquifers at small scales proved to play an important role at larger scales [*Siirila and Maxwell*, 2012a, 2012b]. Interestingly, this effect was observed for only very small increments in local dispersion ($\alpha_T = 0.1$ (mm), equivalent to the amount of local dispersion in Case D1 in this analysis). In contrast, in this analysis, the possible particle jump behavior due to local dispersion is only observed when local dispersion is 2 orders of magnitude larger ($\alpha_T = 10$ mm). It is possible that the degree which local dispersion affects the BTC is sensitive to the structure of the ln(K) field (i.e., a true Gaussian at a variance of 3.61 (-) versus a truncated Gaussian at a variance of 5.29 (-) as simulated here). Regardless, the effect of local dispersion is a topic worth further investigation in hydrogeology as we show it greatly affects the BTC shape.

3.3. Evaluation of Local Peak Slopes

Figures 12 and 13 respectively show calculated slopes for major local peaks and significant local peaks as a function of dimensionless travel distance DI_x^{-1}. Slopes are determined using the cutoff and running variance methodology, as described in section 2.4 and Appendix B, and are shown in different subplots for the four cases of local dispersion (rows, Figures 12 and 13) and heterogeneity models (columns, Figures 12 and 13). Differences in ε are denoted by color (see key in subplot a), and within each ε realizations 1–3 are represented by different symbols.

3.3.1. General Trends in Slope, Comparison of Major Local Peaks and Significant Local Peaks

In general, the most noted trend for both major and significant local peaks (Figures 12 and 13, respectively) within each combination of heterogeneity model, anisotropy ratio, and degree of local dispersion is the general decrease and eventual stabilization of the slope, as dimensionless travel distance increases. In other words, the receding limbs of local peaks are very steep initially and become less steep as more integral scales are traveled. An example of this trend is shown in Figure 10b, where the singular major local peak slope, s, of this particular simulation is noted, and decreases with the evolution of BTC travel distance. This is most evident for significant local peaks (Figure 13), where s trends downward for all DI_x^{-1}; in contrast, for major local peaks (Figure 12) the trend is not as pronounced as more integral scales are traveled, as it tends to reach some asymptote. To explain this behavior, it is necessary to revisit the conceptual model of aquifer sampling, and to embed s within a framework of a mass transfer model.

In these numerical simulations, s represents the rate of mass discharge leaving the plane (computed in double log space), and should not be confused with the rate at which the solute is moving. Any previous rates at which the solute moved can only be inferred relative to the local peak's location in the BTC. The relative location of local peak s in the BTC (i.e., early or late times) are not differentiated in Figure 12 or 13 for the sake of brevity, although this separation could prove to be interesting for future work. We would like to note that in general, the majority of local peaks occur on the general decent of the falling limb of the BTC (although some exceptions occur). Examples are shown in the BTCs of Figures 3 and 9a, where visually the majority of local peaks in the curve occur at times after the global peak of the breakthrough has occurred. In other words, the portions of the plume resulting in local peaks are generally arriving at the plane with correspondingly longer travel times than the global peak breakthrough point. The combination of these local peak transport characteristics (delayed breakthrough time denoted by the position in the curve, but with high breakthrough slopes) indicate two things: (1) that these portions of the plume were once traveling slowly, resulting in the delayed breakthrough time, and (2) that these portions of the plume are later traveling quickly, resulting in the high slope value.

Regarding the overall trend of s decreasing with increasing travel distance, recall that after short travel distances (and low DI_x^{-1}) only a small portion of the aquifer has been sampled and a high probability of
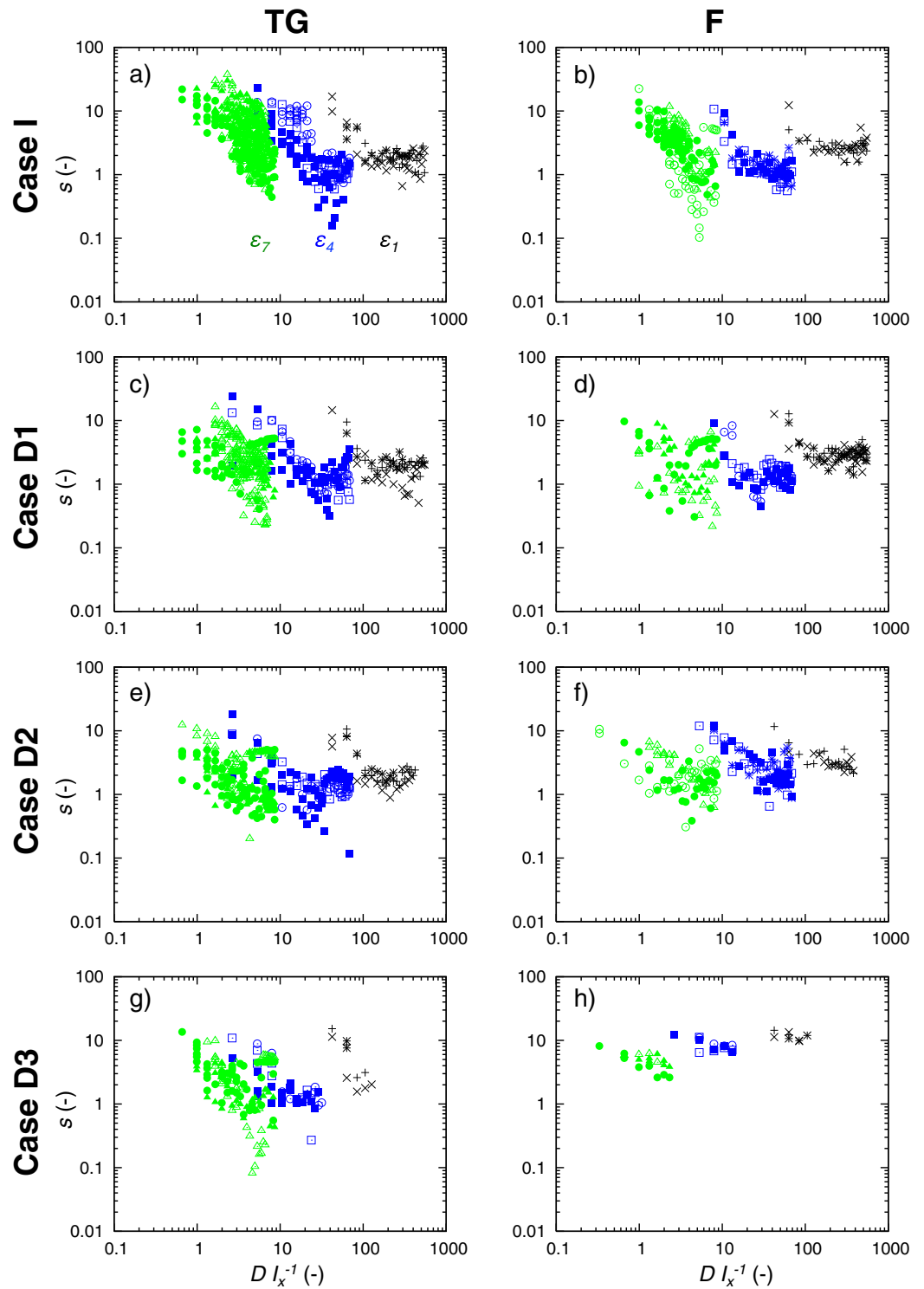
Figure 12. Major local peaks slopes as a function of dimensionless travel distance for different cases of local dispersivity (rows) and heterogeneity models (columns). Statistical anisotropy cases are distinguished by color (ε_1, ε_4, ε_7; see sub-plot a) for three realizations each (denoted by different symbols).

continuous, fast pathways from the source to the plane exist. Thus, the presence of high s values at this travel distance (for both major local peaks and significant local peaks) is merely indicative of the fast mass transfer rates leaving the plane due to this connectivity between the source and the plane. As shown by our numerical results, the presence of high s values at longer travel distances (and high DI_x^{-1}) where a larger
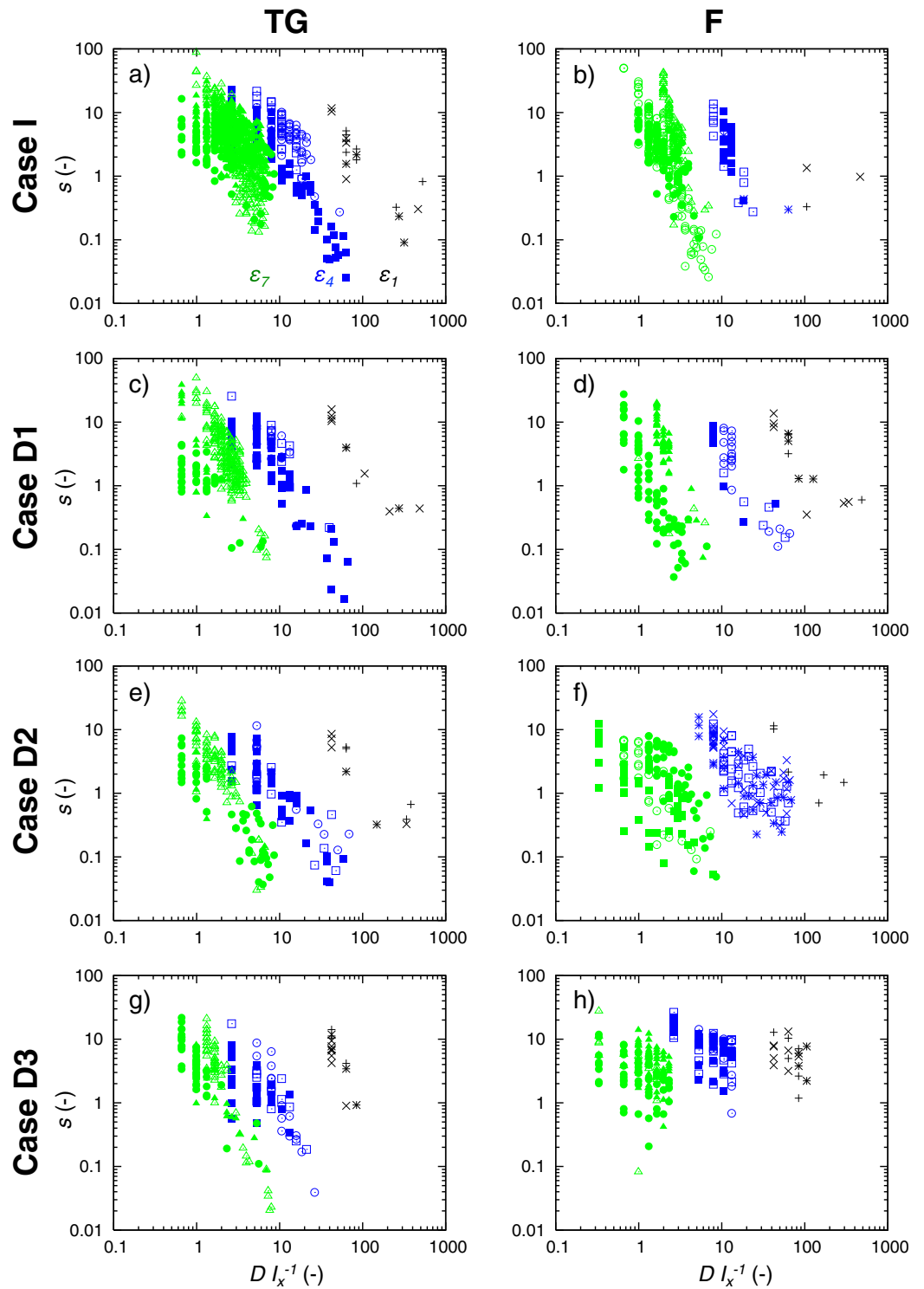
Figure 13. Significant local peaks slopes as a function of dimensionless travel distance for different cases of local dispersivity (rows) and heterogeneity models (columns). Statistical anisotropy cases are distinguished by color (ε_1, ε_4, ε_7; see sub-plot a) for three realizations each (denoted by different symbols).

portion of the aquifer has been sampled and fast pathways between the source and plane are less probable, results in a less profound impact as travel distances are greater. As stated above, the presence of local peaks after the global peak of the BTC is indicative of solute rerouting from slow to fast pathways in the aquifer. The impact is simply less profound as travel distances increase.

Again, this affects the bulk of the plume and more localized parcels of solute differently. As discussed in section 3.2.1, smaller parcels of the solute are indicative of smaller, localized peaks in the BTC (by our definition, significant local peaks) whereas the bulk of the plume will appear as larger maxima in the BTC (by our definition, major local peaks). Major local peaks decrease with greater DI_x^{-1} (Figure 12) and then reach a quasi-steady state value of s whereas significant local peaks s trends towards zero (Figure 13). The point where the s of significant local peaks trends towards zero and the s of major local peaks no longer changes coincides with the same times in which the monopeak regime is approached (see Figures 6 and 7) and where more Fickian-like behavior is expected. Although we could validate this conceptual model with the local peak statistics alone, we also see agreement with respect to trends in s.

The evolution of s as a function of travel distance also sheds a new light on previous efforts to identify the nature of s. Our results show that the magnitude and meaning of s must be assessed only in conjunction with the plume's proximity to the monopeak regime, otherwise the quantity of s is arbitrary. The physical drivers which affect significant and major local peak s (i.e., rerouting of fast pathways or the bulk movement of the plume) also explain why there is a large span of s in the significant local peak results (ranging over 4 orders of magnitude). For major local peaks, our results show that the small range of s for power law tails previously reported (i.e., ranging between 1 and 3.5) [*Tsang*, 1995; *Haggerty et al.*, 2000; *Zhang et al.*, 2007; *Pedretti et al.*, 2013; *Zhang et al.*, 2013] may be a limiting range given the variable range of s for heterogeneous aquifers, depending on travel distance relative to I, and depending on the proximity to monopeak regime. The need to discuss s with reference to something such as relative travel distance to I is analogous to well-documented discussion on assessing the Fickian regime relative to the number of I traveled, as high as tens to hundreds of meters from the source [e.g., *Matheron and De Marsily*, 1980; *Gelhar and Axness*, 1981; *Dagan*, 1982].

Another distinction with this methodology and with traditional analyses of BTC slopes is that as we show here, there is a significant difference between the average slope in a BTC and the local slopes visible immediately after each local peak (s). In many cases, the local peak slope is much higher than the global slope. For example, the illustrative ε_7 BTC in Figure 10a (green line) contains 20 major local peaks, with s ranging from 1.7 to 14.3 and with the average local peak s equaling 6.6. In contrast, the global slope of the BTC is much less steep, closer to 1.0.

3.3.2. Effect of Anisotropy on Slope

In general, the aforementioned s-DI_x^{-1} trend is true for all anisotropy ratios, ε. The range, or variance of s along this trend, however, is sensitive to ε. For most scenarios (Figures 12 and 13), the smallest anisotropy ratio, ε_7, has the most variability in s and the highest anisotropy ratio, ε_1, has the least variability. This finding is in agreement with previous studies, which found that connectivity is the hydrodynamic parameter that most influences late-time BTC behavior [*Zinn and Harvey*, 2003; *Willmann et al.*, 2008; *Pedretti et al.*, 2013]. In a hydrofacies investigation of the impact of mean lengths on power law late-time tails, *Zhang et al.* [2013] found that increasing the horizontal mean length (equivalent to decreasing ε) only shifted the BTC arrival time, while increasing the vertical mean length (equivalent to increasing ε) resulted in a longer tail. In their sensitivity analysis, the thickness of floodplain layers controls late-time BTC shape more than statistical anisotropy.

For major local peaks, the quasi-steady state s value reached as more integral scales are traveled is not sensitive to ε. For most cases, the s value after a large number of integral scales have been traveled with respect to each ε scenario is approximately 0.5. For cases with less major local peaks to be analyzed (e.g., Figure 12h), it is difficult to speculate if these slopes are representative of late times, and thus if a steady state s can be determined. Recall from above that the significant local peaks do not reach a quasi-steady state s value, and in general trend toward zero for all ε.

3.3.3. Effect of Heterogeneity Model on Slope

Differences in heterogeneity models (TG versus F columns Figures 12 and 13) affect significant local peaks more than major local peaks. With the exception of one case (F-Case D3, Figure 12h) differences between truncated Gaussian and facies model major local peak slopes are negligible. The range of significant local peak slopes differ given the heterogeneity model used, although there does not seem to be a clear trend suggesting why. In general, these differences are small when compared to sensitivity in other parameters affecting the slope, such as anisotropy.

3.3.4. Effect of Local Dispersion on Slope

In general, the effect of local dispersion (rows, columns, Figures 12 and 13) does not play a major role on the evolution of the s-DI_x^{-1} trend. *Pedretti et al.* [2013] found that an increase in local dispersivity affects particle arrival times, but does not affect the BTC s. Instead, their results show that s is more sensitive to aquifer stratification and connectivity. This is in agreement with our results, which show that the number of peaks, and the shape of the BTC is sensitive to local dispersion (see discussion in section 3.1.4), but does not necessarily affect the rate of particle transfer at the plane.

4. Conclusions

The traditional approach in BTC analysis considers that the curve has distinct rising and receding limbs, thus displaying a single unique peak. A number of studies have shown that real aquifer BTCs may not follow this pattern, so that the actual curve may contain a number of local peaks. With recent advances in data analysis, we are able to reconstruct high-resolution BTCs from a finite number of particles with low error. By comparing the mean reconstructed curve with the uncertainty about the mean, we quantitatively demonstrate that the presence of multiple peaks in BTCs is more the rule rather than the exception for individual plumes resulting from a fixed size source. A conceptual model is proposed showing how preferential flow, shearing events, and aquifer sampling create local peaks, followed by a quantitative analysis of how different modeling parameters and heterogeneity models affect these processes and thus the formation of local peaks. A number of high-resolution numerical simulations were performed using three-dimensional synthetic aquifer in order to study the number of BTC local peaks, their duration, and corresponding slope. Sensitivity to the travel distance, heterogeneity model of ln(K), statistical anisotropy, and Peclet number were explored. As shown in this study, the presence of multiple local peaks is particularly true for highly anisotropic media and after small travel distances. As distance evolves, transport tends to more Fickian-like behavior and the traditional, single peak curve prevails. Other key findings include:

1. The analysis of the transport connectivity index, CI, reveals that connectivity increases with statistical anisotropy and decreases with travel distance, consistent with the parameters characterizing the development of a monopeak BTC. Our results show that simulations with higher transport connectivity display more local peaks. Furthermore, the truncated Gaussian model generates random fields with better well-connected heterogeneous structures when compared to a facies model, especially for high Pe.

2. The number of local peaks (both major local peaks and significant local peaks) is clearly affected by both travel distance (negative correlation) and by the degree of statistical anisotropy (positive correlation), but also by the heterogeneity model used. For the same global statistics, the truncated Gaussian models result in a larger number of major local peaks and significant local peaks as compared to facies models.

3. The increase in local dispersion tends to lessen the effect of the other parameters by producing a homogenization of concentrations via enhanced mixing. In general the smaller the Pe value, the smaller the transport connectivity index, CI, and the smaller the number of local peaks. For the smallest Pe scenario simulated, we actually see an increase in the number of local peaks, potentially due to solutes jumping from areas of high to low K and vice versa.

4. There is a significant difference between the average slope in a BTC and the local slopes visible immediately after each local peak (s), the latter being much higher than the global slope. In general, such local slopes are very steep initially and become less steep as more integral scales are traveled, associated with the different mass transfer processes taking place between the high-flow and low-flow areas as a function of distance. Statistical anisotropy mainly affects the range of s values more than other parameters (Pe, model of heterogeneity), a factor probably associated with the degree of connectivity of the aquifer. For major local peaks, s tends to a constant value after long travel distances, a value that seems not to be related to anisotropy but somehow to the heterogeneity model used in the simulations. In contrast, significant local peak slopes trend downward as travel distance increases, consistent with the disappearance and smoothening of sharp local peaks in the BTC.

Local peaks may be important in assessing environmental concentrations in human and environmental risk analysis, as recent work has shown that time dependence in the entire concentration signal may be imperative in accurate hazard assessment and management. For example, overlooking local peaks in BTCs may

lead to discrepancies in exposure concentrations, depending on the magnitude and duration. As we show here, knowledge of the frequency and slope of local peaks in a BTC may be linked to physical aquifer parameters, and may inform modeling and site characteristics efforts.

Appendix A

Consider a series of travel times $\{t_1, \ldots, t_n\}$ obtained at a given control plane during a particle tracking simulation. When all particles share the same mass, the kernel density estimator of the normalized BTC is:

$$p(t) = \frac{1}{np\ h} \sum_{i=1}^{n} K_{KDE}\left(\frac{t-t_i}{h}\right) \tag{A1}$$

where h is the bandwidth of the bin size that ultimately controls the degree of smoothing and K_{KDE} [T^{-1}] is the kernel density estimator. Large h values will smooth out the solution and small h values will generate excessive noise, providing jagged curves (the extreme case would be a Dirac delta function). *Fernàndez-Garcia and Sanchez-Vila* [2011] demonstrated that the optimal bandwidth h_{opt} [T] is proportional to some negative power of the number of particles, actually $h_{opt} = C\ np^{-1/5}$, where C is a constant that mainly depends on the curvature of the BTC (norm of the second derivative). Then, the standard deviation of the kernel density estimate p approaches in the limit to

$$\sigma_p(t) = n^{-2/5} \sqrt{\|K_p\|_2^2 p(t) C^{-1}} \tag{A2}$$

where $\|K_p\|$ is the second norm of the kernel density function. Assuming a Gaussian shape of the kernel density function

$$K_{KDE}(u) = \frac{1}{\sqrt{2\pi}} \exp\left(-\frac{u^2}{2}\right) \tag{A3}$$

then the norm becomes

$$\|K_p\|_2^2 = \int K_p(u)^2 du = (2\pi)^{-1} \sqrt{\pi} \tag{A4}$$

With the use of equation (A2), the coefficient of variation, $CV = 100\ \sigma_p$ [%], is calculated to ensure low error due to the use of the KDE and np. As shown in Figure A1, for the example BTC in Figure 3, extremely low CV values are present for the $np = 400,000$ simulation, except for very late times where concentrations are low. For less jagged BTCs, the CV is generally even lower.
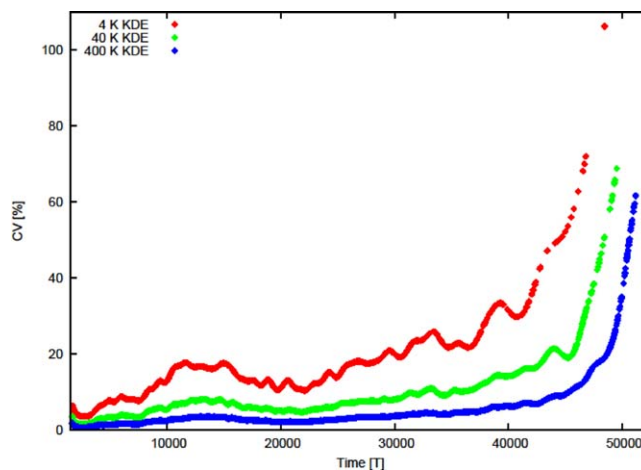

Figure A1. Coefficient of variation of an example KDE reconstructed BTC (same as Figure 3) for varying number of particles (see color key).

Appendix B

As stated in section 2.4, to ensure that the tail end of the slope is not oversampled, the final sampling time of the local peak slope (t_{sample}) is not necessarily t_f. For example, if the slope changes very drastically as t approaches t_f, the portion of the local peak may not be representative of the overall local peak slope and should be excluded from the calculation. To do so, first the arithmetic running average of the slope, $s_{avg}(t_n)$, is calculated as a function of time, t_n, within this

duration (beginning at $t = t_i$ and until $t = t_f$) as:

$$s_{avg}(t_n) = \frac{1}{t_n - t_i} \sum_{j=i+1}^{j=n} s_j \; (t_j - t_{j-1}) \tag{B1a}$$

$$s_j = \frac{\log m_j - \log m_{j-1}}{\log t_j - \log t_{j-1}} \tag{B1b}$$

where $\{t_1, t_2, \ldots\}$ are the sampling times of the BTC, s_j is the slope in the jth time interval $[t_{j-1}, t_j]$, and m_j is the mass discharged at time t_j. To determine t_{sample}, the arithmetic running variance of the slope, $\sigma_s^2(t_n)$, is required, as it is a measure of the slope's dispersion from the average value. Similar to $s_{avg}(t_n)$, $\sigma_s^2(t_n)$ is calculated as a function of time within this duration (beginning at $t = t_i$ and until $t = t_f$) as:

$$\sigma_s^2(t_n) = \frac{1}{t_n - t_i} \sum_{j=i+1}^{j=n} \left(s_{avg}(t_j) - s_j\right)^2 (t_j - t_{j-1}) \tag{B2}$$

Once $\sigma_{s,t}^2$ has exceeded a certain threshold, $s_{avg}(t_n)$ is no longer representative of the tail edge of the local peak, and therefore should not be included in the sample. In this case, t_{sample} is defined as the time at which this threshold is exceeded (see Figure 4d). For our simulations, a threshold variance of 0.01 (-) was found to accurately represent the slope without oversampling the tail. Two additional constraints were added to determine $s_{avg}(t_n)$: (1) if after 20 time steps for significant local peaks or if after 100 time steps for major local peaks, $\sigma_{s,t}^2$ exceeded the 0.01 (-) cutoff, or (2) if after sampling the entire duration of local peak (i.e., from at $t = t_i$ and until $t = t_f$) the 0.01 (-) cutoff was not exceed, $t_{sample} = 20$ for significant local peaks or $t_{sample} = 100$ for major local peaks. Given these two conditions, we found an accurate sampling of the local peak slope. Note that similar to the determination of the local peak cutoffs (section 2.3), the determination of t_{sample} will likely be data set specific. Lastly, to ensure statistical significance, only BTCs where at least 95% of the original mass is retained are analyzed. For brevity, the value of $s_{avg}(t_n)$ when $t_n = t_{sample}$ are referred to as simply s, and are the values reported in section 3.2.

Notation

BTC   breakthrough curve
TG   truncated Gaussian model
F   facies model
KDE   kernel density estimator
UAB   universal adaptive bandwidth
SLP   significant local peak
MLP   major local peak

Symbols

P_{1-25} Plane number [-]
$P_{\Delta x}$ distance between each plane [L]
K hydraulic conductivity [$L\,T^{-1}$]
I integral scale [L]
ε anisotropy ratio [-]
θ porosity [-]
Δh change in head [L]
J gradient [-]
K_G geometric mean of K [$L\,T^{-1}$]
σ^2 variance of ln(K) [-]
$K_{H,F,L}$ hydraulic conductivity of facies [$L\,T^{-1}$]
$P_{H,F,L}$ proportion of facies [-]
r_{HL}, r_{LH} facies off-diagonal transition probabilities [-]
Pe peclet number [-]
α_L, α_T longitudinal and transverse dispersivity [L]

np	number of particles [-]
CI	connectivity indicator [-]
t_{50}, t_5	times which 50% and 5% of the plume mass pass the plane [T]
s	slope [-]
m	mass discharge [$M\ T^{-1}$]
t	time [T]
t_i	time at which slope changes from positive to negative [T]
t_f	time at which slope changes from negative to positive [T]
t_{sample}	final sampling time of local peak [T]
$s_{avg}(t_n)$	arithmetic running average of s [-]
$\sigma_s^2(t_n)$	arithmetic running variance of the slope [-]
D	x direction travel distance from the source to plane [L]
h	bandwidth of the bin size [L]
h_{opt}	optimal bandwidth of the bin size [L]
K_{KDE}	kernel density estimator [T^{-1}]
$\sigma_p(t)$	standard deviation of the kernel density estimate [T^{-1}]
$\|K_p\|$	second norm of the kernel density function
CV	coefficient of variation [-]

References

Andersson, P., R. Nordqvist, T. Persson, C. O. Eriksson, E. Gustafsson, and T. Ittner (1993), Dipole tracer experiment in a low-angle fracture zone at Finnsjön—Results and interpretation. The Fracture Zone Project—Phase 3, *SKB Tech. Rep. 93-26*, Swed. Nucl. Fuel and Waste Manage., Stockholm.

Ashby, S. F., and R. D. Falgout (1996), A parallel multigrid preconditioned conjugate gradient algorithm for groundwater flow simulations, *Nucl. Sci. Eng.*, *124*(1), 145–159.

Becker, M. W., and A. M. Shapiro (2000), Tracer transport in fractured crystalline rock: Evidence of nondiffusive breakthrough tailing, *Water Resour. Res.*, *36*(7), 1677–1686.

Bellin, A., A. J. Valocchi, and A. Rinaldo (1991), Double peak formation in reactive solute transport in one-dimensional heterogeneous porous media, *Quaderni Dipartimento IDR 1*, pp. 1–35, Dipartimento di Ing. Civ. et Ambientale, Univ. degli Studi di Trento, Trento, Italy.

Berman, E. S. F., M. Gupta, C. Gabrielli, T. Garland, and J. J. McDonnell (2009), High-frequency field-deployable isotope analyzer for hydrological applications, *Water Resour. Res.*, *45*, W10201, doi:10.1029/2009WR008265.

Bijeljic, B., and M. J. Blunt (2006), Pore-scale modeling and continuous time random walk analysis of dispersion in porous media, *Water Resour. Res.*, *42*, W01202, doi:10.1029/2005WR004578.

Bolster, D., Y. Méheust, T. Le Borgne, J. Bouquain, and P. Davy (2014), Modeling preasymptotic transport in flows with significant inertial and trapping effects—The importance of velocity correlations and a spatial Markov model, *Adv. Water Resour.*, *70*, 89–103.

Boso, F., A. Bellin, and M. Dumbser (2013), Numerical simulations of solute transport in highly heterogeneous formations: A comparison of alternative numerical schemes, *Adv. Water Resour.*, *52*, 178–189.

Carle, S., and G. Fogg (1996), Transition probability-based indicator geostatistics, *Math. Geol.*, *28*(4), 453–476.

Carle, S., and G. Fogg (1997), Modeling spatial variability with one and multidimensional continuous-lag Markov chains, *Math. Geol.*, *29*(7), 891–918.

Carle, S. F. (1999), *T-PROGS: Transition Probability Geostatistical Software*, Univ. of Calif., Davis, Calif.

Cherry, J. A., R. W. Gillham, and J. F. Barker (1984), *Groundwater Contamination. Studies in Geophysics*, pp. 46–64, U.S. Natl. Res. Counc., Natl. Acad. Press, Washington, D. C.

Coppola, A., V. Comegna, A. Basile, N. Lamaddalena, and G. Severino (2009), Darcian preferential water flow and solute transport through bimodal porous systems: Experiments and modelling, *J. Contam. Hydrol.*, *104*(1–4), 74–83.

Dagan, G. (1982), Stochastic modeling of groundwater by unconditional and conditional probabilities: 2. The solute transport, *Water Resour. Res.*, *18*(4), 835–848.

Dagan, G. (1988), Time-dependent macrodispersion for solute transport in anisotropic heterogeneous aquifers, *Water Resour. Res.*, *24*(9), 1491–1500.

Day-Lewis, F. D., J. W. Lane Jr., and S. M. Gorelick (2004), Combined interpretation of radar, hydraulic, and tracer data from a fractured-rock aquifer near Mirror Lake, New Hampshire, USA, *Hydrogeol. J.*, *14*(1–2), 1–14.

Dentz, M., and B. Berkowitz (2003), Transport behavior of a passive solute in continuous time random walks and multirate mass transfer, *Water Resour. Res.*, *39*(5), 1111, doi:10.1029/2001WR001163.

Dentz, M., and D. Bolster (2010), Distribution-versus correlation-induced anomalous transport in quenched random velocity fields, *Phys. Rev. Lett.*, *105*(24), 244–301.

Farrell, J., and M. Reinhard (1994), Desorption of halogenated organics from model solids, sediments, and soil under unsaturated conditions. 2. Kinetics, *Environ. Sci. Technol.*, *28*(1), 63–72.

Fernàndez-Garcia, D., and X. Sanchez-Vila (2011), Optimal reconstruction of concentrations, gradients and reaction rates from particle distribution, *J. Contam. Hydrol.*, *120–121*, 99–114.

Fernàndez-Garcia, D., T. H. Illangasekare, and H. Rajaram (2004), Conservative and sorptive forced-gradient and uniform flow tracer tests in a three-dimensional laboratory test aquifer, *Water Resour. Res.*, *40*, W10103, doi:10.1029/2004WR003112.

Fernàndez-Garcia, D., G. Llerar-Meza, and J. J. Gómez-Hernández (2009), Upscaling transport with mass transfer models: Mean behavior and propagation of uncertainty, *Water Resour. Res.*, *45*, W10411, doi:10.1029/2009WR007764.

Frost, L. H., and C. C. Davison (1994), Summary of the fracture zone 3 groundwater tracer test program at the underground research laboratory, *Rep. TR-617*, Appl. Geosci. Branch, Whiteshell Lab., Pinawa, Manitoba, Canada.

Gelhar, L. W., and C. C. Axness (1981), Stochastic analysis of macrodispersion in three-dimensionally heterogeneous aquifers, *Rep. H8*, 140 pp., Geophys. Res. Cent., Hydrol. Res. Program, New Mexico Inst. of Min. and Technol., Socorro, N. M.

Göppert, N., and N. Goldschneider (2008), Solute and colloid transport in karst conduits under low- and high-flow conditions, *Ground Water*, *46*(1), 61–68.

Haggerty, R., S. A. McKenna, and L. C. Meigs (2000), On the late-time behavior of tracer test breakthrough curves, *Water Resour. Res.*, *36*(12), 3467–3479.

Haggerty, R., S. M. Wondzell, and M. A. Johnson (2002), Power-law residence time distribution in the hyporheic zone of a 2nd-order mountain stream, *Geophys. Res. Lett.*, *29*(13), doi:10.1029/2002GL014743.

Hammond, G. E., P. C. Lichtner, and R. T. Mills (2014), Evaluating the performance of parallel subsurface simulators: An illustrative example with PFLOTRAN, *Water Resour. Res.*, *50*, 208–228, doi:10.1002/2012WR013483.

Jones, J. E., and C. S. Woodward (2001), Newton-Krylov-multigrid solvers for large-scale, highly heterogeneous, variably saturated flow problems, *Adv. Water Resour.*, *24*(7), 763–774.

Kinzelbach, W. (1988), The random walk method in pollutant transport simulation, in *Advances in Analytical and Numerical Groundwater Flow and Quality Modelling, NATO ASI Ser. C*, vol. 224, edited by E. Custodio et al., pp. 227–246, Springer, Netherlands.

Kitanidis, P. K. (1994), The concept of the dilution index, *Water Resour. Res.*, *30*(7), 2011–2026.

Knudby, C., and J. S. Carrera (2005), On the relationship between indicators of geostatistical, flow and transport connectivity, *Adv. Water Resour.*, *28*(4), 405–421.

Kollet, S. J., and R. M. Maxwell (2006), Integrated surface-groundwater flow modeling: A free-surface overland flow boundary condition in a parallel groundwater flow model, *Adv. Water Resour.*, *29*(7), 945–958.

Kollet, S. J., R. M. Maxwell, C. S. Woodward, S. Smith, J. Vanderborght, H. Vereecken, and C. Simmer (2010), Proof of concept of regional scale hydrologic simulations at hydrologic resolution utilizing massively parallel computer resources, *Water Resour. Res.*, *46*, W04201, doi:10.1029/2009WR008730.

Koltermann, C. E., and S. M. Gorelick (1996), Heterogeneity in sedimentary deposits: A review of structure-imitating, process-imitating, and descriptive approaches, *Water Resour. Res.*, *32*(9), 2617–2658.

Kumar, V., F. P. J. D. Barros, M. Schuhmacher, D. Fernàndez-Garcia, and X. Sanchez-Vila (2013), Dynamic interactions between hydrogeological and exposure parameters in daily dose prediction under uncertainty and temporal variability, *J. Hazard. Mater.*, *263*(Part 1), 197–206.

LaBolle, E. M., G. E. Fogg, and A. F. B. Tompson (1996), Random-walk simulation of transport in heterogeneous porous media: Local mass-conservation problem and implementation methods, *Water Resour. Res.*, *32*(3), 583–593.

Le Borgne, T., M. Dentz, and E. Villermaux (2013), Stretching, coalescence, and mixing in porous media, *Phys. Rev. Lett.*, *110*, 204501.

Mallants, D., M. Vanclooster, M. Meddahi, and J. Feyen (1994), Estimating solute transport in undisturbed soil columns using time-domain reflectometry, *J. Contam. Hydrol.*, *17*, 91–109.

Matheron, G., and G. De Marsily (1980), Is transport in porous media always diffusive?, *Water Resour. Res.*, *16*(5), 901–917.

Maxwell, R. M. (2010), *SLIM-FAST: A User's Manual*, vol. 4, Int. Ground Water Model. Cent., Golden, Colo.

Michalak, A. M., and P. K. Kitanidis (2000), Macroscopic behaviour and random-walk particle tracking of kinetically sorbing solutes, *Water Resour. Res.*, *36*(8), 2133–2146.

Moreno, L., and C. F. Tsang (1991), Multiple-peak response to tracer injection tests in single fractures: A numerical study, *Water Resour. Res.*, *27*(8), 2143–2150.

Navarre-Sitchler, A. K., R. M. Maxwell, E. R. Siirila, G. E. Hammond, and P. C. Lichtner (2013), Elucidating geochemical response of shallow heterogeneous aquifers to CO_2 leakage using high-performance computing: Implications for monitoring of CO_2 sequestration, *Adv. Water Resour.*, *53*, 45–55.

Pedretti, D., and D. Fernàndez-Garcia (2013), An automatic locally-adaptive method to estimate heavily-tailed breakthrough curves from particle distributions, *Adv. Water Resour.*, *59*, 52–65.

Pedretti, D., D. Fernàndez-Garcia, D. Bolster, and X. Sanchez-Vila (2013), On the formation of breakthrough curves tailing during convergent flow tracer tests in three-dimensional heterogeneous aquifers, *Water Resour. Res.*, *49*, 4157–4173, doi:10.1002/wrcr.20330.

Pedretti, D., D. Fernandez-Garcia, X. Sanchez-Vila, D. Bolster, and D. A. Benson (2014), Apparent directional mass-transfer capacity coefficients in three-dimensional anisotropic heterogeneous aquifers under radial convergent transport, *Water Resour. Res.*, *50*, 1205–1224, doi:10.1002/2013WR014578.

Quinodoz, H. A. M., and A. J. Valocchi (1993), Stochastic analysis of the transport of kinetically sorbing solutes in aquifers with randomly heterogeneous hydraulic conductivity, *Water Resour. Res.*, *29*(9), 3227–3240.

Rodak, C., S. E. Silliman, and D. Bolster (2013), Time-dependent health risk from contaminated groundwater including use of reliability, resilience, and vulnerability as measures, *J. Am. Water Resour. Assoc.*, *50*(1), 14–28.

Rubin, Y. (2003), *Applied Stochastic Hydrology*, Oxford Univ. Press, Oxford, U. K.

Rubin, Y., A. Sun, R. M. Maxwell, and A. Bellin (1999), The concept of block effective macrodispersivity and a unified approach for grid-scale and plume-scale dependent transport, *J. Fluid Mech.*, *395*, 161–180.

Rudolph, D. L., R. G. Kachanoski, M. A. Celia, D. R. LeBlanc, and J. H. Stevens (1996), Infiltration and solute transport experiments in unsaturated sand and gravel, Cape Cod, Massachusetts: Experimental design and overview of results, *Water Resour. Res.*, *32*(3), 519–532.

Salamon, P., D. Fernàndez-Garcia, and J. J. Gómez-Hernández (2006), A review and numerical assessment of the random walk particle tracking method, *J. Contam. Hydrol.*, *87*(3–4), 277–305.

Schumer, R., D. A. Benson, M. M. Meerschaert, and B. Baeumer (2003), Fractal mobile/immobile solute transport, *Water Resour. Res.*, *39*(10), 1296, doi:10.1029/2003WR002141.

Siirila, E. R., and R. M. Maxwell (2012a), A new perspective on human health risk assessment: Development of a time dependent methodology and the effect of varying exposure durations, *Sci. Total Environ.*, *431*, 221–232.

Siirila, E. R., and R. M. Maxwell (2012b), Evaluating effective reaction rates of kinetically driven solutes in large-scale, statistically anisotropic media: Human health risk implications, *Water Resour. Res.*, *48*, W04527, doi:10.1029/2011WR011516.

Siirila, E. R., A. K. Navarre-Sitchler, R. M. Maxwell, and J. E. McCray (2012), A quantitative methodology to assess the risks to human health from CO_2 leakage into groundwater, *Adv. Water Resour.*, *36*, 146–164.

Siirila-Woodburn, E. R., and R. M. Maxwell (2015), A heterogeneity model comparison of highly resolved statistically anisotropic aquifers, *Adv. Water Resour.*, *75*, 53–66, doi:10.1016/j.advwatres.2014.10.011.

Thorbjarnarson, K. W., and D. M. Mackay (1994), A forced-gradient experiment on solute transport in the Borden aquifer: 2. Transport and dispersion of the conservative tracer, *Water Resour. Res.*, *30*(2), 385–399.

Tompson, A. F. B., R. Ababou, and L. W. Gelhar (1989), Implementation of the three-dimensional turning bands random field generator, *Water Resour. Res.*, *25*(10), 2227–2243.

Trefry, M. G., F. P. Ruan, and D. McLaughlin (2003), Numerical simulations of preasymptotic transport in heterogeneous porous media: Departures from the Gaussian limit, *Water Resour. Res.*, *39*(3), 1063, doi:10.1029/2001WR001101.

Tsang, Y. W. (1995), Study of alternative tracer tests in characterizing transport in fractured rocks, *Geophys. Res. Lett.*, *22*(11), 1421–1424.

Tyler, S. W., J. S. Selker, M. B. Hausner, C. E. Hatch, T. Torgersen, C. E. Thodal, and S. G. Schladow (2009), Environmental temperature sensing using Raman spectra DTS fiber-optic methods, *Water Resour. Res.*, *45*, W00D23, doi:10.1029/2008WR007052.

Vanderborght, J., H. Vereecken (2001), Analyses of locally measured bromide breakthrough curves from a natural gradient tracer experiment at Krauthausen, *Journal of Contaminant Hydrology*, *48*, 23–43.

Werth, C. J., J. A. Cunningham, P. V. Roberts, and M. Reinhard (1997), Effects of grain-scale mass transfer on the transport of volatile organics through sediments: 2. Column results, *Water Resour. Res.*, *33*(12), 2727–2740.

Willmann, M., J. Carrera, and X. Sánchez-Vila (2008), Transport upscaling in heterogeneous aquifers: What physical parameters control memory functions?, *Water Resour. Res.*, *44*, W12437, doi:10.1029/2007WR006531.

Zarlenga, A., I. Janković, and A. Fiori (2013), Advective transport in heterogeneous formations: The impact of spatial anisotropy on the breakthrough curve, *Transp. Porous Media*, *96*(2), 295–304.

Zhang, Y., and M. M. Meerschaert (2011), Gaussian setting time for solute transport in fluvial systems, *Water Resour. Res.*, *47*, W08601, doi: 10.1029/2010WR010102.

Zhang, Y., D. A. Benson, and B. Baeumer (2007), Predicting the tails of breakthrough curves in regional-scale alluvial systems, *Ground Water*, *45*(4), 473–484.

Zhang, Y., C. T. Green, and G. E. Fogg (2013), The impact of medium architecture of alluvial settings on non-Fickian transport, *Adv. Water Resour.*, *54*, 78–99.

Zinn, B., and C. F. Harvey (2003), When good statistical models of aquifer heterogeneity go bad: A comparison of flow, dispersion, and mass transfer in connected and multivariate Gaussian hydraulic conductivity fields, *Water Resour. Res.*, *39*(3), 1051, doi:10.1029/2001WR001146.

Erratum

1. Table 2 was incorrectly formatted in the following ways: (1) A second instance of "Anisotropy Ratio" appeared underneath the same header. (2) Parentheses needed to be placed around the units "m d^{-1}" in three places toward the end of Table 2 to match the same formatting as the line that starts with "Geometric mean of K," which appears correctly as "(m d^{-1})".

2. The reference and citations for *Siirila-Woodburn and Maxwell* [2014] throughout the paper have been updated to reflect the current publication year. This version may be considered the authoritative version of record.

SIIRILA-WOODBURN ET AL.   2152